Heliyon 10 (2024) e33814

Contents lists available at ScienceDirect

Heliyon

journal homepage: www.cell.com/heliyon

Research article

Structural and theoretical exploration of a multi-methoxy chalcone: Synthesis, quantum theory, electrostatics, molecular packing, DFT analysis, and in-silico anti-cancer evaluation

Fares Hezam Al-Ostoot [a,*], P. Akhileshwari [b], Vivek Hamse Kameshwar [c], D. V. Geetha [d], Majed S. Aljohani [e], Hussam Y. Alharbi [e], Shaukath Ara Khanum [a], M.A. Sridhar [f,**]

[a] Department of Biochemistry, Faculty of Education & Science, Albaydha University, Albaydha, Yemen
[b] PG Department of Physics, JSS College of Arts, Commerce and Science, Ooty Road, Mysuru 570025, Karnataka, India
[c] Department of Biotechnology, Adichunchanagiri School of Natural Sciences, ACU-CRI, Adichunchanagiri University, B.G. Nagara- 571448, Mandya, Karnataka, India
[d] Physics Department, Mysore University School of Engineering, Manasagangotri, Mysuru 570006, India
[e] Department of Chemistry, Faculty of Science, Taibah University, Yanbu, Saudi Arabia
[f] Department of Studies in Physics, Manasagangotri, University of Mysore, Mysuru 570 006, India

ARTICLE INFO

Keywords:
Chalcone
Quantum theory
Molecular electrostatic
Molecular packing
DFT calculations
Anti-cancer activity

ABSTRACT

This study explores the pharmacological potential of chalcones through a multidisciplinary approach, including synthesis, quantum theory, molecular electrostatics, and density functional theory (DFT) calculations. The synthesized compound, analyzed via single crystal X-ray diffraction, crystallized in the triclinic system (space group P-1) with C–H···O interactions stabilizing its structure. Hirshfeld surface analysis confirms these interactions, with H–H contacts dominating (45.1 %). Molecular electrostatics analysis reveals charge distribution, and a 3.10 eV HOMO-LUMO energy gap indicates bioactivity. Molecular docking identifies the compound (**3a**) showed a maximum G_{score} of HTNF-α (−9.81 kcal/mol); Tubulin (−7.96 kcal/mol); COX2 (−7.88 kcal/mol), EGFR (−6.72 kcal/mol), and VEGFR1(-2.50 kcal/mol). Where compound (**3c**) showed maximum binding at the putative binding site with dock scores for VEGFR2 (−9.24 kcal/mol). This research not only advances molecular science but also holds promise for diverse applications, including drug design. The significance of this study lies in its comprehensive exploration of the pharmacological potential of chalcones using a multidisciplinary approach. Through the integration of synthesis, quantum theory, molecular electrostatics, and density functional theory (DFT) calculations, we have extensively explored the structural and biochemical characteristics of these compounds. This investigation has revealed valuable insights that have the potential to lead to significant advancements in the fields of molecular science and drug design. Moreover, the molecular docking studies shed light on the compound's interaction with various biological targets. The significant binding affinities observed for these targets underscore the potential therapeutic relevance of the synthesized compound in diverse disease conditions.

* Corresponding author.
** Corresponding author.
E-mail addresses: Faresalostoot@gmail.com (F.H. Al-Ostoot), mas@physics.uni-mysore.ac.in (M.A. Sridhar).

https://doi.org/10.1016/j.heliyon.2024.e33814
Received 15 February 2024; Received in revised form 8 June 2024; Accepted 27 June 2024
Available online 2 July 2024
2405-8440/© 2024 The Author(s). Published by Elsevier Ltd. This is an open access article under the CC BY-NC license (http://creativecommons.org/licenses/by-nc/4.0/).

1. Introduction

As of the latest update, cancer remains a substantial worldwide health issue, characterized by the uncontrolled growth and spread of abnormal cells in the human system [1]. Researchers, specialists, and politicians are consistently striving to enhance cancer prevention and diagnosis measures through ongoing research and breakthroughs in therapy [2]. Continual cancer research is enhancing our comprehension of the fundamental biology of various types of cancer, hence aiding the progress of precise treatments such as targeted medications and immunotherapies [3]. Furthermore, advancements in early detection techniques and precision treatment are enhancing the results for several individuals [4]. Cancer is a multifaceted disease, and tumours can exhibit substantial differences among patients and even within the same patient. In addition, the primary challenge in cancer treatment isn't found in the drug's potential itself but rather in the heterogeneity of cancer [5]. Drug resistance is also a phenomenon in which cancer cells gradually become resistant to conventional treatments, resulting in therapy failure and the progression of the disease. Additionally, this can encompass the spread of cancer to other parts of the body, the harmful consequences on the body, adverse reactions, and the timely identification of the disease [6].

Chalcone and its analogues belong to a group of organic substances that possess a basic aromatic ketone that is joined by a three-carbon α,β-unsaturated carbonyl system between two aromatic rings [7–9]. Researchers have extensively studied chalcone derivatives for their potential therapeutic applications in various diseases [10]. There are various ways to produce chalcone derivatives, including the Claisen-Schmidt condensation process, which involves an aromatic ketone and an aromatic aldehyde in the presence of a base [11,12]. These compounds have attracted significant attention due to their various biological actions, such as anti-oxidant [13], anti-cancer [14], anti-inflammatory [15], anti-viral, and anti-microbial properties [16,17], Fig. 1. The structural diversity of these compounds allows for systematic structure-activity relationship (SAR) studies to optimize their biological activities and selectivity [18]. Therefore, the specific biological activities and properties of chalcone derivatives can vary widely depending on their chemical structure and substitution patterns [19].

Several studies have demonstrated the potential anti-cancer effects of chalcones, highlighting their significance in cancer prevention and treatment [20]. These chemicals have exhibited diverse modes of action that may delay the proliferation of cancer cells, induce apoptosis (programmed cell death), and affect tumor formation [21,22], by interfering with essential cellular processes, such as cell cycle regulation and DNA replication [23]. In addition, chalcones possess anti-inflammatory properties which are often associated with cancer development and can help suppress inflammation-induced tumor growth [24,25]. Additionally, they can obstruct the development of new blood vessels (angiogenesis), a critical process for tumor growth and spread [26,27].

Continuing our ongoing research into the development and analysis of new derivatives, we have effectively synthesized and characterized the title compound in question through spectroscopic methods, considering its extensive biological properties [28–30]. Additional validation of the molecular framework was obtained by single-crystal X-ray diffraction investigations. Furthermore, in order to examine the ligand's 3-D geometric interactions with the targeted human tyrosine-protein kinase VEGFR-1, 2, EGFR, Tubulin,

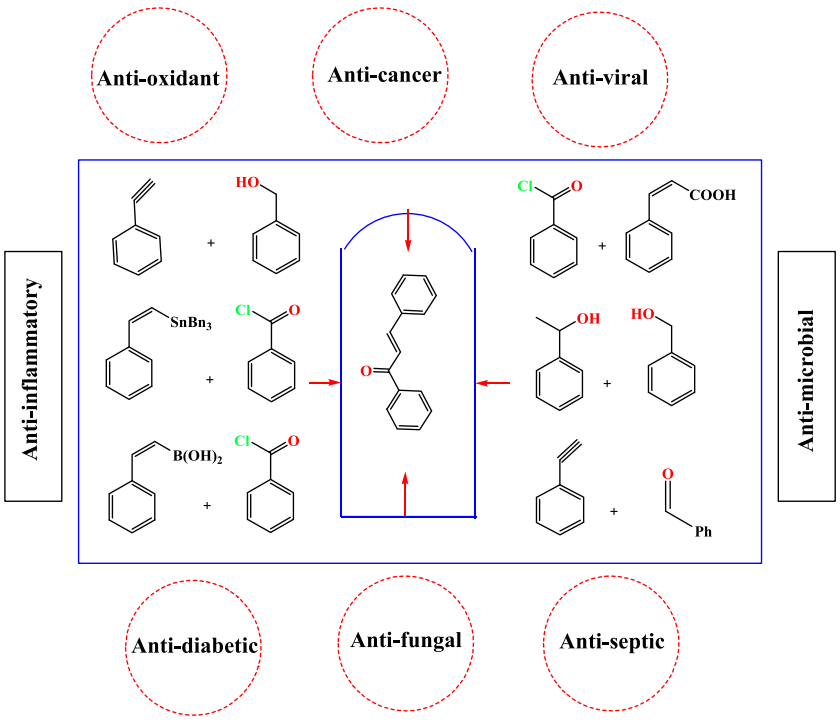

Fig. 1. Many chalcones obtained via coupling reactions and their biological applications.

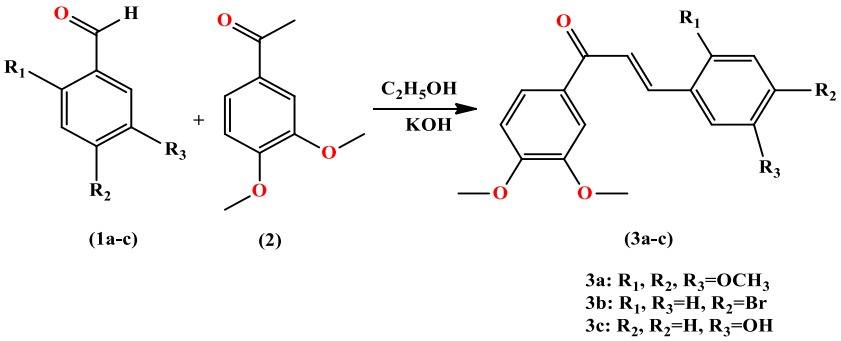

Scheme 1. Synthesis of Multi-Methoxy Chalcones (**3a-c**).

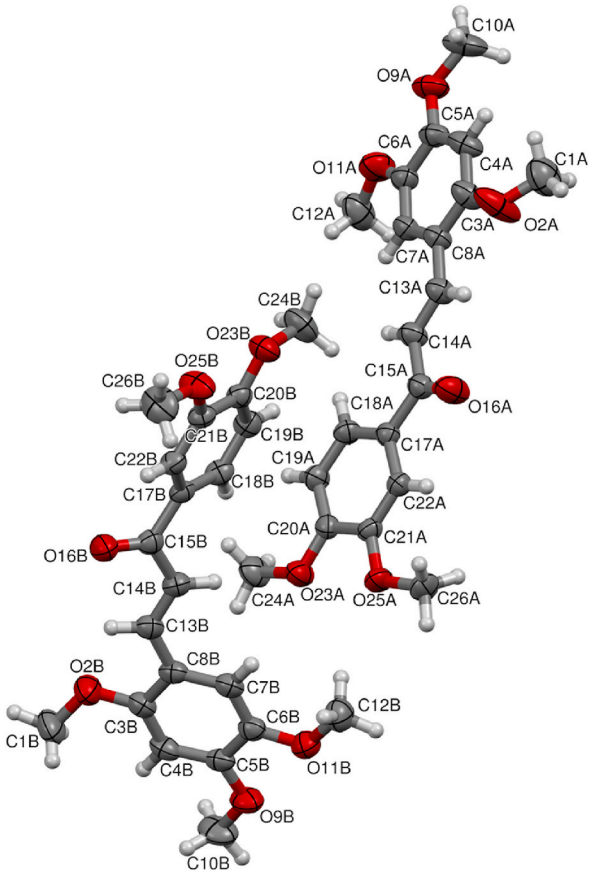

Fig. 2. Plot of thermal ellipsoids of the compound with 50 % probability.

HTNF-α, and COX2 comprehensive molecular docking studies have been carried out. This kinase is pivotal in regulating crucial biological processes such as angiogenesis, vascular development, vascular permeability, and embryonic hematopoiesis.

2. Experimental procedure

2.1. Materials and methods

All molecular-grade experimental supplies were acquired from Sigma-Aldrich. The confirmation of reaction completion and the synthesis of the target compound (**3**) was accomplished through thin-layer chromatography (TLC) on silica gel 60 F_{254}, utilizing a mixture of hexane and ethyl acetate in a 3:1 ratio. Spectroscopic data, encompassing ^{1}H and ^{13}C NMR, were collected using Bruker Advancer 400 MHz and 300 MHz NMR spectrometers in DMSO. Mass spectra was produced with a VG70-70H spectrophotometer,

Table 1
Crystal data and structure refinement details of (**3a**).

CCDC number	1943076
Empirical formula	C_{20} H_{22} O_6
Formula weight	358.38
Temperature	293(2) K
Wavelength	0.71075 Å
θ range for above	3.00°–27.50°
Crystal system, Space group	Triclinic, P-1
Cell parameters	a = 11.8054(19)Å, b = 12.332(2)Å, c = 14.291(3)Å, α = 72.139°, β = 69.142°, γ = 76.583°
Volume	1832.8(6) $Å^{-3}$
Z	4
Density(calculated)	1.299 Mg m^{-3}
Absorption coefficient	0.096 mm^{-1}
F_{000}	760
Crystal size	0.23 mm × 0.22 mm × 0.21 mm
θ range for data collection	3.04° to 27.48°
Index ranges	$-15 \leq h \leq 12$ $-11 \leq k \leq 16$ $-18 \leq l \leq 18$
Reflections collected	10636
Independent reflections	8156 [$R_{int} = 0.0256$]
Refinement method	Full matrix least-squares on F^2
Data/restraints/parameters	8156/0/479
Goodness-of-fit on F^2	1.044
Final [$I > 2\sigma(I)$]	R1 = 0.0693, w$R2$ = 0.1454
R indices (all data)	R1 = 0.1266, w$R2$ = 0.1694

Table 2
Selected bond lengths of the compound (**3a**).

	Length(Å)			Length(Å)	
Atoms	XRD	DFT	Atoms	XRD	DFT
C1A-O2A	1.359(5)	1.418	C14A-C15A	1.470(4)	1.477
C3A-O2A	1.370(4)	1.364	C15A-O16A	1.225(3)	1.236
C3A-C4A	1.382(4)	1.403	C15A-C17A	1.488(3)	1.498
C3A-C8A	1.385(3)	1.412	C17A-C18A	1.380(3)	1.396
C4A-C5A	1.375(4)	1.394	C17A-C22A	1.407(3)	1.410
C1B–O2B	1.417(3)	1.414	C14B–C15B	1.463(3)	1.482
C3B–C4B	1.386(4)	1.402	C15B–O16B	1.230(3)	1.233
C3B–C8B	1.398(3)	1.410	C15B–C17B	1.486(3)	1.495
C4B–C5B	1.379(4)	1.395	C17B–C18B	1.376(3)	1.395
C5B–O9B	1.348(3)	1.359	C17B–C22B	1.397(3)	1.410

Table 3
Selected bond angles of the compound (**3a**).

	Angle(°)			Angle(°)	
Atoms	XRD	DFT	Atoms	XRD	DFT
C1A-O2A-C3A	120.2(3)	119.3	O2B–C3B–C4B	123.5(2)	122.8
O2A-C3A-C4A	122.1(3)	122.7	O2B–C3B–C8B	115.6(2)	116.5
O2A-C3A-C8A	117.1(3)	116.6	C3B–C8B–C13B	120.9(2)	120.1
C3A-C8A-C13A	120.3(2)	119.6	C3B–C8B–C7B	117.5(2)	117.7
C3A-C8A-C7A	117.9(2)	117.6	C3B–O2B–C1B	118.8(2)	119.1
C7A-C6A-O11A	125.0(3)	125.6	C7B–C6B–O11B	125.0(2)	125.6
C7A-C8A-C13A	121.8(2)	122.7	C7B–C8B–C13B	121.6(2)	122.1
O9A-C5A-C4A	124.9(3)	124.6	O9B–C5B–C4B	125.4(2)	124.3
O9A-C5A-C6A	115.5(3)	115.4	O9B–C5B–C6B	115.1(2)	115.6
O11A-C6A-C5A	115.8(2)	115.4	O11B–C6B–C5B	115.6(2)	115.5

presenting significant fragments and their respective intensities in brackets. The results of the elemental analysis showed a variation from the values that were calculated of only 0.4 %. A double-beam UV–visible spectrophotometer from Shimadzu UV-1800 was used to record the UV–visible spectrum.

Table 4
Selected torsion angles of the compound (**3a**).

	Angle(°)			Angle(°)	
Atoms	XRD	DFT	Atoms	XRD	DFT
O2A-C3A-C4A-C5A	−178.9(3)	178.4	O2B–C3B–C4B–C5B	178.6(2)	179.6
O2A-C3A-C8A-C13A	−2.5(4)	2.0	O2B–C3B–C8B–C13B	2.0(4)	1.4
O2A-C3A-C8A-C7A	178.9(2)	−179.3	O2B–C3B–C8B–C7B	−179.6(2)	−179.7
C3A-C4A-C5A-C6A	0.2(4)	0.0	C3B–C4B–C5B–C6B	1.1(4)	0.1
C3A-C4A-C5A-O9A	−178.6(3)	179.7	C3B–C4B–C5B–O9B	−178.5(2)	179.8
C13A-C14A-C15A-C17A	178.5(2)	179.3	C13B–C14B–C15B–C17B	−167.6(3)	−172.3
C15A-C17A-C22A-C21A	179.3(2)	177.0	C15B–C17B–C22B–C21B	−179.4(2)	−179.8
C18A-C17A-C22A-C21A	−0.3(4)	−0.2	C18B–C17B–C22B–C21B	−1.0(4)	−1.1
O23A-C20A-C21A-C22A	−177.3(2)	−178.5	C24B–O23B–C20B–C19B	2.5(4)	2.1
O25A-C21A-C22A-C17A	178.7(2)	−179.3	O23B–C20B–C21B–C22B	178.4(2)	−178.5

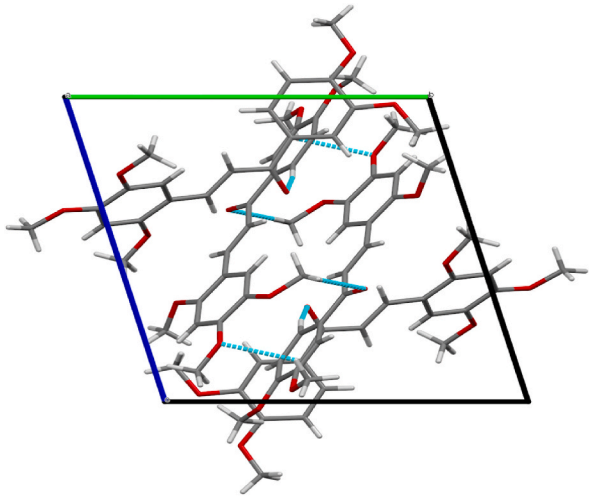

Fig. 3. Molecular packing of the compound when viewed down *a* axis.

Table 5
Hydrogen bond geometry.

Atoms	D-H (Å)	H … A (Å)	D-A (Å)	D-H … A(°)
C1A-H1A3 … O23B[a]	0.96	2.35	3.507(4)	164
C12A-H12A … O16A[b]	0.96	2.54	3.502(4)	178
C12B–H12D … O25A[b]	0.96	2.60	3.466(4)	151
C13A-H13A … O2A[c]	0.96	2.38	2.743(3)	103
C13A-H13A … O16A[c]	0.96	2.44	2.786(3)	102
C18A-H18A … O16B[d]	0.93	2.59	3.467(4)	158

[a] : 1-*x*, -*y*, 1-*z*.
[b] : 1-*x*, 1-*y*, 1-*z*.
[c] : Intramolecular interaction.
[d] : 1-*x*, 1-*y*, -*z*.

Table 6
C–H … π interactions involved in the molecular structure.

C···H	cgJ	H … cg (Å)	H ⊥ (Å)	γ (o)	C–H … cg (o)	C … cg(Å)	C–H … π (o)
C26A-H26B	cg4[a]	2.91	2.82	14.50	132	3.631(3)	42

[a] : 2 − *x*, 1 − *y*, −*z*.

Table 7
π - π stacking interactions involved in the molecular structure.

CgI	cgI	cgI–cgJ (Å)	α (∘)	β (∘)	γ (∘)	cgI ⊥ (Å)	cgJ ⊥ (Å)
cg1	cg2[a]	3.7468(17)	10.98(12)	6.5	14.0	3.6357(10)	3.7230(10)
cg2	cg1[a]	3.7469(17)	10.98(12)	14.0	6.5	3.7230(10)	3.6358(10)
cg3	cg4[b]	4.8456(18)	73.76(12)	6.6	69.1	1.7307(11)	−4.8139(10)
cg4	cg2[c]	4.5541(18)	73.76(12)	16.9	70.8	−1.6784(10)	−4.8910(11)

[a] : 1-*x*, 1-*y*, 1-*z*.
[b] : *x*, *y*, *z*.
[c] : 1-*x*, 1-*y*, -*z*.

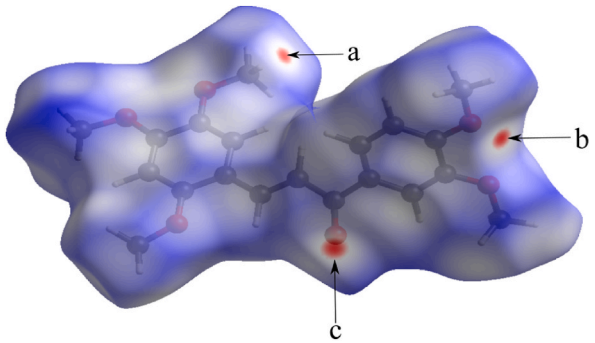

Fig. 4. Hirshfeld surface mapped over d_{norm}.

*2.2. **Synthesis** of Multi-Methoxy Chalcones (**3a-c**)*

The synthesis of the target compounds (**3a-c**) was accomplished through a base-catalyzed Claisen-Schmidt condensation reaction. Trimethoxybenzaldehyde (**1** in Scheme 1, 0.010 mol) and 3,4-dimethoxyacetophenone (**2**, 0.010 mol) were mixed in 10 ml of ethyl alcohol and stirred at 25 °C for 20 min. Subsequently, the reaction mixture was stirred and 7 ml of potassium hydroxide solution was added dropwise. Using hexane:ethyl acetate (7:3) as the eluent, the reaction was tracked using TLC for 4 h until it completely clouded over. After it was finished, the mixture was added to 2 ml of hydrochloric acid in ice-cold water. To achieve a crude product, the final solid was filtered, treated with ice-cold water, and then dried. Slow-release mode system recrystallization with ethanol yielded the title compound of multi-methoxy chalcone derivatives (**3a-c**) in the form of colorless rectangular block-shaped crystals (Scheme 1) [8,9].

2.3. Spectral analysis

2.3.1. (E)-1-(3,4-dimethoxyphenyl)-3-(2,4,5-trimethoxyphenyl)prop-2-en-1-one (3a)

Yield: 77 %. M.P. 102–104 °C; **IR (KBr, cm^{-1}):**1025 cm^{-1} (C–O) group of –OCH_3, 1400-1600cm^{-1} (aromatic C═C), 1593 cm^{-1} (C═C olefin), 1655 cm^{-1} (C═O) group, 2930 cm^{-1} (C–H of –OCH_3) and 3084 cm^{-1} (sp^2 olefinic bond). **^{1}HNMR (DMSO-d_6), δ (ppm)**: 3.81 (s, 6H, –OCH_3), 3.84 (s, 6H, –OCH_3), 3.95 (s, 3H, –OCH_3), 6.54 (s, 1H, Ar–H), 6.82 (s, 1H, *J* = 16 Hz, Ar–H), 7.18 (d, 1H, Ar–H), 7.32 (s, 1H, Ar–H), 7.48 (d, 1H, *J* = 16 Hz, Ar–H), 7.91 (d, 1H, *J* = 16 Hz, =CH), 8.39 (d, 1H, *J* = 16Hz, =CH). **^{13}C NMR (DMSO-d_6) δ:** 56.32, 115.16, 117.61, 118.67, 121.20, 122.25, 123.83, 130.14, 131.93, 136.50, 134.83, 149.20, 153.61, 158.17, 187.42. **LC-MS *m/z*** 359 (M+1). Anal. Cal. data for $C_{20}H_{22}O_6$ (358): C, 67.03; H, 6.19; Found: C, 67.00; H, 6.15.

2.3.2. 1-(3,4-dimethoxyphenyl)-3-(4-bromophenyl) prop-2-en-1-one (3b)

Yield: 80 %. M.P. 92–94 °C; **IR (KBr, cm^{-1}):**1025 cm^{-1} (C–O) group of –OCH_3, 1450-1650cm^{-1} (aromatic C═C), 1590 cm^{-1} (C═C olefin), 1650 cm^{-1} (C═O) group, 2930 cm^{-1} (C–H of –OCH_3) and 3085 cm^{-1} (sp^2 olefinic bond). **^{1}HNMR (DMSO-d_6), δ (ppm)**: 3.77–3.84 (s, 6H, -2OCH_3), 7.06 (s, 1H, Ar–H), 7.57–7.67 (d, 4H, *J* = 16 Hz, Ar–H), 7.81–7.83 (d, 2H, *J* = 16 Hz, Ar–H), 7.90 (d, 1H, *J* = 16 Hz, =CH), 7.98 (d,1H, *J* = 16Hz, =CH). **^{13}C NMR (DMSO-d_6) δ:** 56.22, 111.12, 123.13, 123.96, 124.18, 130.78, 131.18, 132.26, 134.57, 142.13, 149.24, 153.75, 187.63. **LC-MS *m/z*** 349 (M+2). Anal. Cal. data for $C_{17}H_{15}BrO_3$ (347): C, 58.84; H, 4.38 Found: C, 58.88; H, 4.39 %.

2.3.3. 1-(3,4-dimethoxyphenyl)-3-(3-hydroxyphenyl) prop–2-en-1-one (3c)

Yield: 94 %. M.P. 114–116 °C; **IR (KBr, cm^{-1}):** 1035 cm^{-1} (C–O) group of –OCH_3, 1600 cm^{-1} (C═C olefin), 1660 cm^{-1} (C═O group), 3530-3598 cm^{-1} (OH group); **^{1}HNMR (DMSO-d_6), δ (ppm)**: 3.83 (s, 6H, -2OCH_3), 6.81 (s, 1H, OH), 7.04–7.87 (m, 7H, Ar–H),

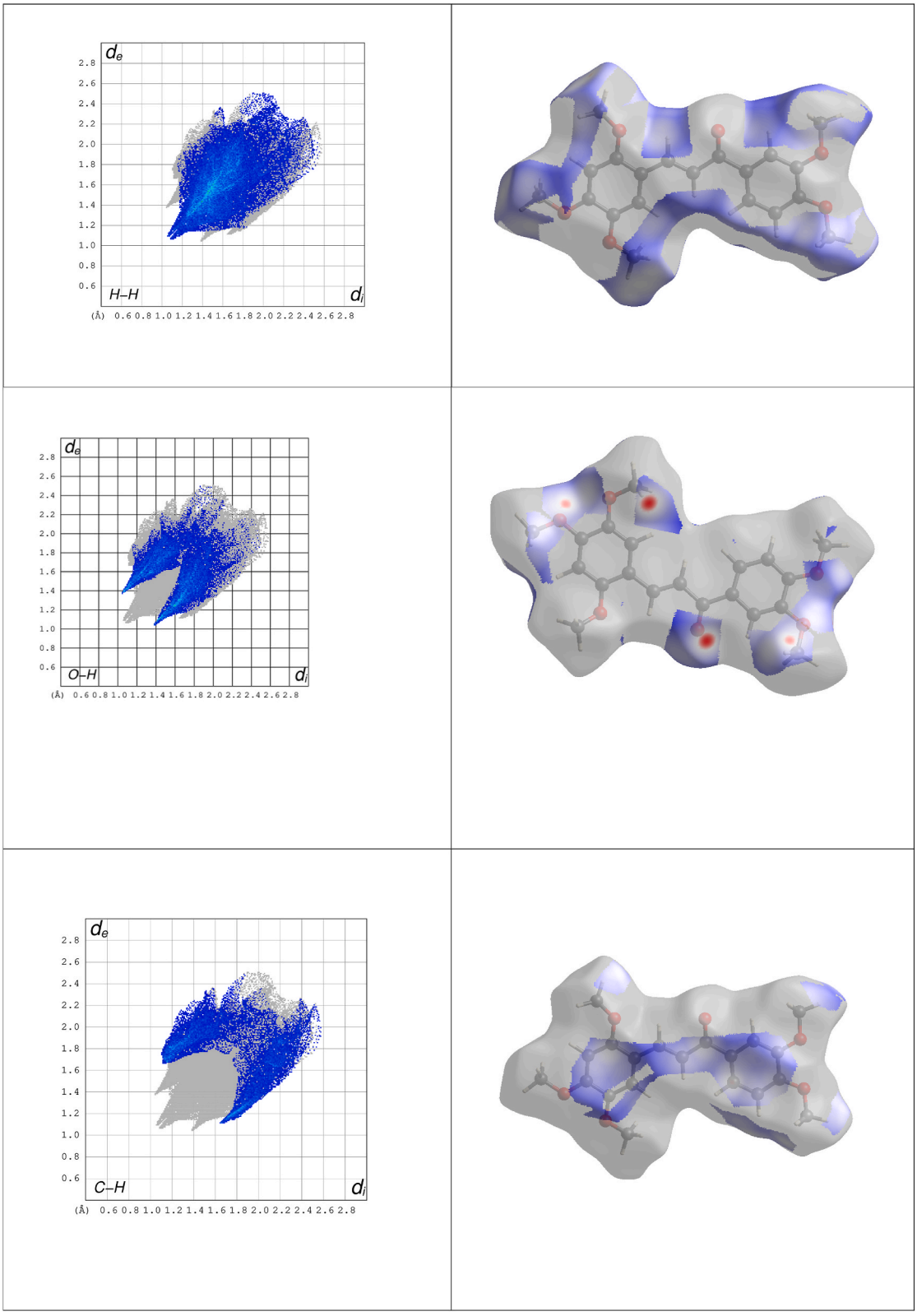

Fig. 5. Fingerprint plots for the resolved into H···H contacts, O···H contacts, and C···H contacts.

Table 8
Percentage contributions to the total Hirshfeld surface area from various intermolecular contacts.

Inter Contacts	Contribution (%)
H–H	45.1
O–H	27.6
C–H	21.1
C–C	5.1

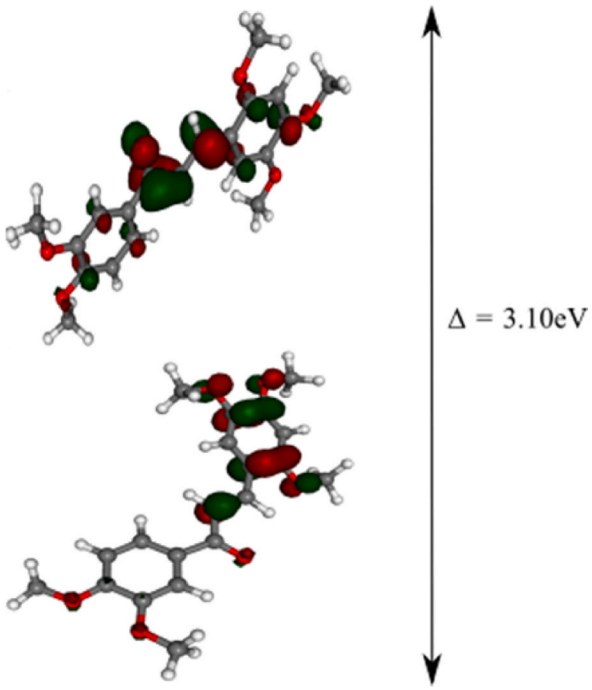

Fig. 6. Frontier molecular orbitals HOMO and LUMO of the compound.

Table 9
Global descriptive parameters.

Parameter	Values	(eV)
E_{HOMO}	−4.83	
E_{LUMO}	−1.73	
Energy Gap (ΔE)	3.10	
Ionization Potential (I)	4.83	
Electron Affinity (E)	1.73	
Chemical Potential (μ)	−3.28	
Electronegativity (χ)	3.28	
Chemical Hardness (η)	1.55	
Electrophilicity (ω)	3.47	

7.61 (d, 1H, $J = 16$ Hz, =CH), 9.61 (d, 1H, $J = 16$Hz, =CH). **^{13}C NMR (DMSO-d_6) δ:** 56.17, 111.11, 115.64, 118.04, 120.26, 122.19, 123.78, 130.27, 130.93, 136.55, 134.77, 149.21, 153.62, 158.16, 187.80. **LC-MS *m/z*** 286 (M+1). Anal. Cal. for $C_{17}H_{16}O_4$ (285): C, 71.85; H, 5.66. Found: C, 71.65; H, 5.49 %.

2.4. In silico studies

In the past few decades, computational chemistry has seen significant advancements in developing novel therapeutics [31–34]. The molecular docking procedure was carried out by Prabhudeva et al. [35]. The PDB IDs for VEGFR1 (3HNG), VEGFR2 (4ASE), EGFR (5 × 2A), Tubulin (5LYJ), HTNF-α (7KP9), and COX2 (3LN1), these coordinates were obtained from the protein data bank. Each protein was created using a set of automated default settings, including automated, required bonds, bond orders, hybridization, explicit hydrogen,

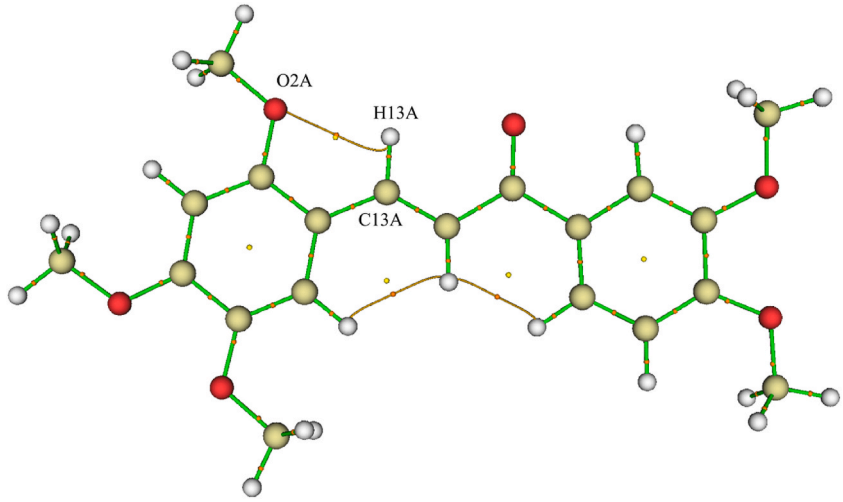

Fig. 7. Intramolecular interactions observed in the compound.

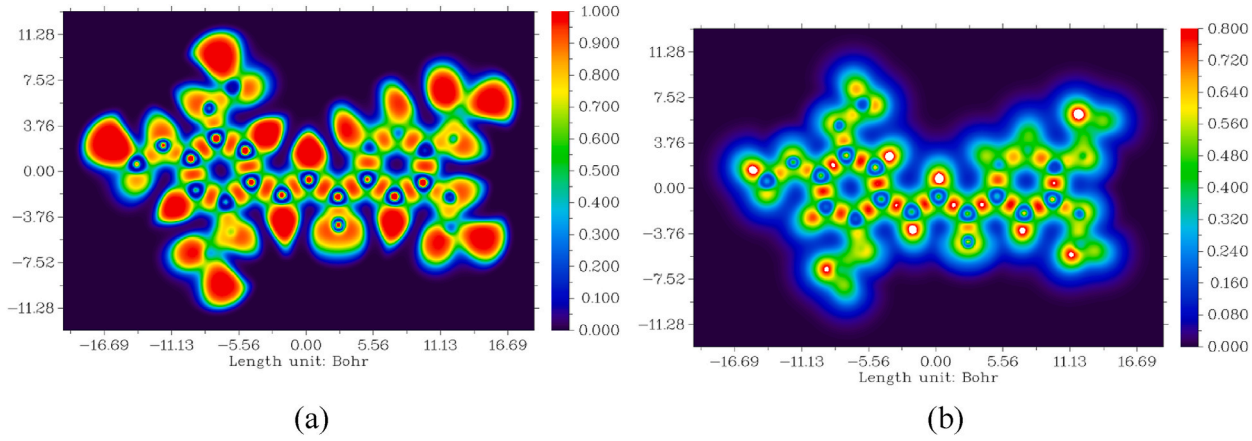

Fig. 8. ELF and LOL of molecule presented in color shade map. (For interpretation of the references to color in this figure legend, the reader is referred to the Web version of this article.)

and charge assignments. Water molecules from proteins were also removed from heteroatoms more than 5 Å away from them. The protein preparation wizard was used to prepare the protein, the catalytic water molecules at the active site were retained, and an OPLS3 force field was applied [36] to the protein for restrain minimization. Root-mean-square deviation (RMSD) was set at 0.30 Å to converge heavy atoms during the pre-processing of the protein before beginning docking in the maestro's prime module. After the protein was ready, a grid generation with a 20 Å separation from the active site was computed. A 2D sketcher was used to create the ligand structure, and OPLS3 was used to compute the energy minimization. It was docked into a receptor grid with a radius of 20 Å using extra-precision docking, and docking calculation was assessed using the docking score [35,37,38].

2.5. MM/GBSA calculation

The stability of the binding and the impact of point mutations on the ligand binding are reflected in the binding energy (ΔG_{Bind}) between a protein and a ligand. The newly created ligand **3(a–c)** was successfully bound to VEGFR1, VEGFR2, EGFR, Tubulin, HTNF-α and COX2 with different affinities. The Prime MM/GBSA module in Mäestro was used in this investigation to predict ΔG_{Bind} [39]. The posture viewer data for the docked complex were posted to the MM/GBSA panel. The force field OPLS3, and the solvation model was VSGB 2.0 applied [40]. $\Delta G_{(bind)}$ was calculated using the equation given below

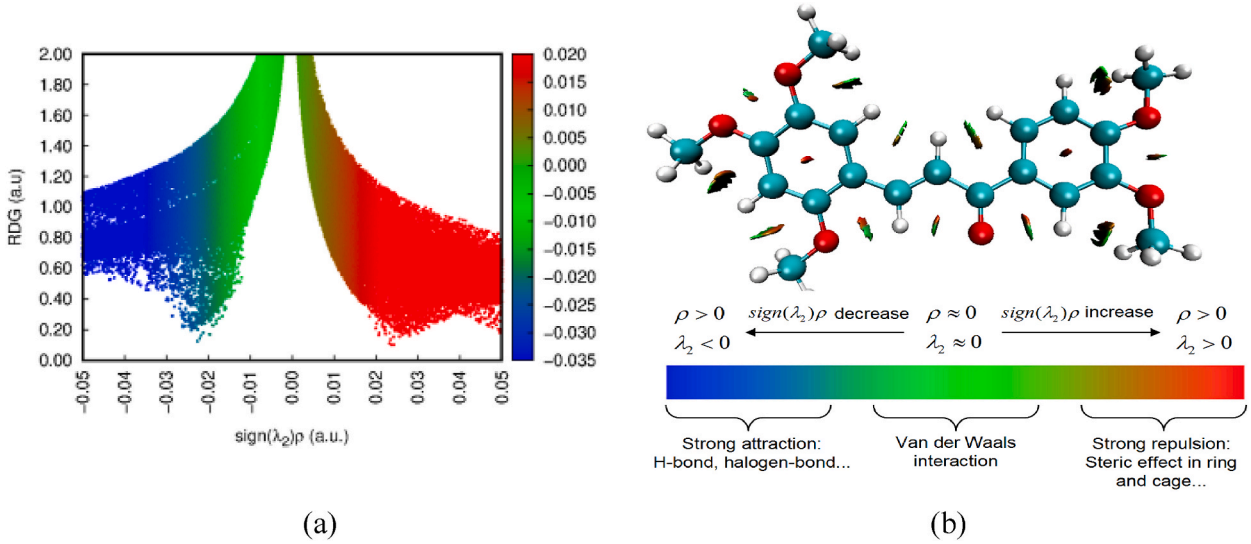

Fig. 9. The 2D scattered plot and RDG isosurfaces of the molecule.

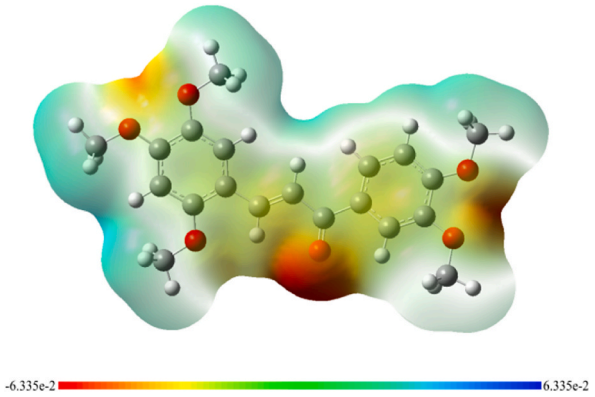

Fig. 10. The MEP plot of the compound.

Table 10
Molecular Docking and MMGBSA ΔG binding (kcal/mol) of synthesized compounds (**3a-c**).

Protein (PDB ID)	Ligand	Molecular Docking (kcal/mol)				MMGBSA ΔG binding (kcal/mol)				
		Docking Score	Glide Energy	Glide Emodel	XP HBond	Bind	Coulomb	Hbond	Lipo	vdW
VEGFR1 (3HNG)	3a	−2.50	−30.53	−33.45	−1.70	−22.26	−18.54	−2.26	−8.47	−21.49
	3b	−0.96	−24.95	−31.56	0.00	−28.24	−4.82	0.00	−8.44	−31.44
	3c	−1.13	−28.31	−33.75	−0.19	−16.68	−6.55	−0.91	−8.49	−20.93
Tubulin (5LYJ)	**3a**	**−7.96**	**−50.68**	**−64.80**	**−0.70**	**−59.57**	**−18.94**	**−0.65**	**−20.01**	**−50.32**
	3b	−7.32	−42.89	−43.71	0.00	−37.70	−2.25	−0.05	−19.69	−54.20
	3c	−7.09	−51.77	−61.50	0.00	−41.44	−7.08	−0.33	−22.81	−58.14
HTNF-α (7KP9)	**3a**	**−9.81**	**−33.92**	**−47.20**	**−1.20**	**−29.02**	**−12.24**	**−0.98**	**−25.27**	**−38.01**
	3b	−9.01	−38.73	−52.73	−0.79	−32.94	−5.11	−1.27	−23.16	−34.77
	3c	−9.18	−45.36	−62.14	−0.70	−40.56	−3.52	−0.58	−26.37	−52.07
COX2 (3LN1)	**3a**	**−7.88**	**−25.32**	**−11.67**	**−0.97**	**−41.49**	**−19.32**	**−1.85**	**−29.94**	**−6.79**
	3b	−8.51	−18.21	−14.60	−0.98	−23.82	−13.54	−1.72	−25.57	−14.59
	3c	−7.84	−42.81	−58.29	−0.12	−31.02	−16.07	−1.19	−28.12	−34.94
EGFR (5 × 2A)	**3a**	**−6.72**	**−48.84**	**−67.31**	**−0.70**	**−5.66**	**−20.29**	**−0.79**	**−19.47**	**−39.72**
	3b	−4.45	−46.47	−55.95	−0.18	−4.59	−24.17	−0.59	−15.84	−41.05
	3c	−6.41	−46.50	−59.71	−1.00	−3.96	−33.44	−1.69	−16.54	−38.56
VEGFR2 (4ASE)	3a	−4.96	−33.59	−34.70	−0.46	−38.20	−6.94	−0.73	−17.41	−38.86
	3b	−7.80	−41.56	−49.13	−0.70	−62.19	−7.84	−0.54	−25.31	−40.47
	3c	**−9.24**	**−36.94**	**−51.51**	**−1.47**	**−61.05**	**−9.90**	**−1.58**	**−26.52**	**−39.07**

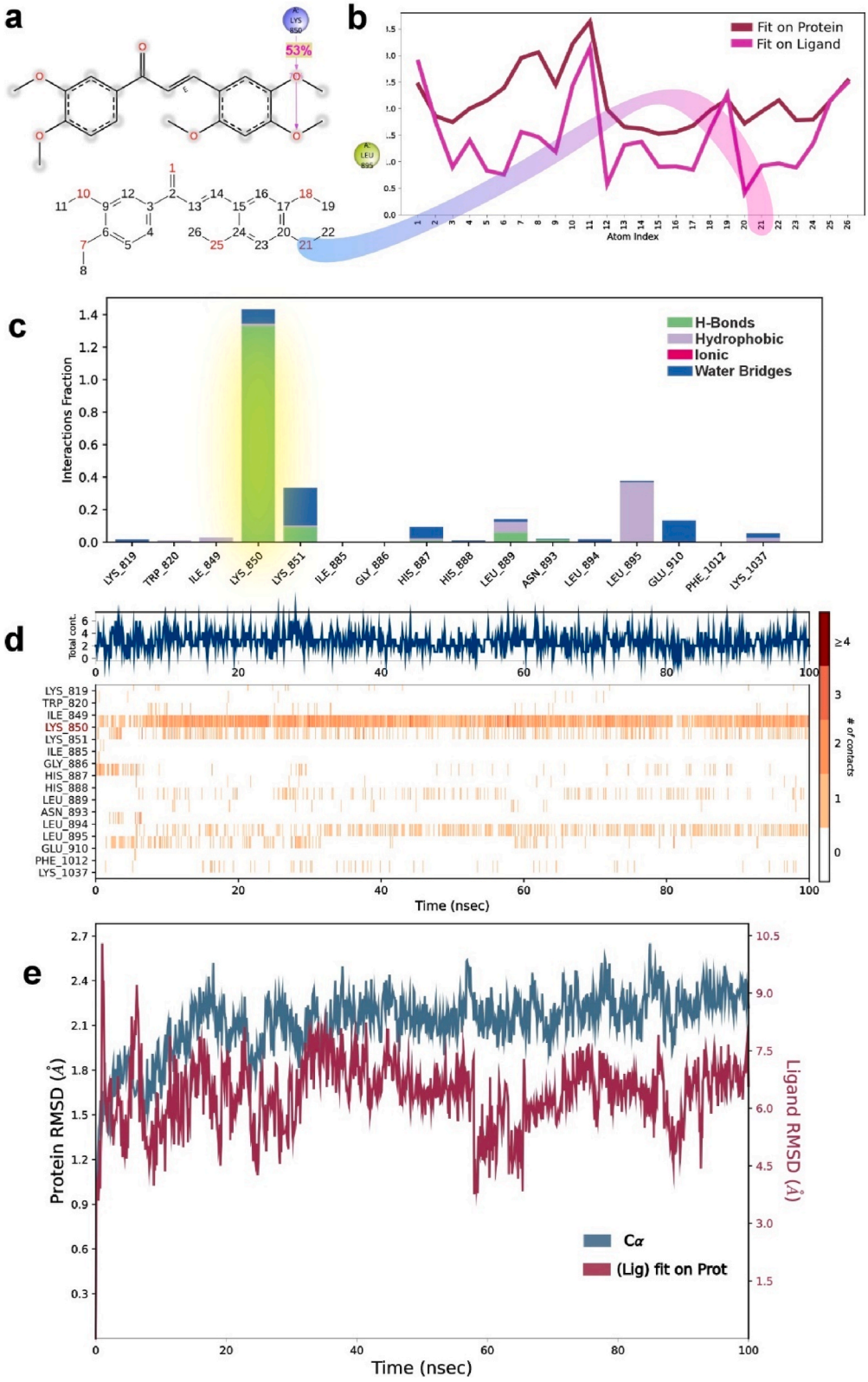

(caption on next page)

Fig. 11. 2D geometrical interactive plot showing interactions of amino acids with compound **3a** in 2D binding view at the potential VEGFR1 binding site **3a** (**a**) and L-RMSF depicting the atoms from the compound **(3a)** interacting with the VEGFR1 throughout the MDSs (**b**) and the type of interaction possessed by the protein-ligand complex is summarized in a normalized stacked bar chart (**c**). The number of contact strengths is color-coded, which represents how well the compound **(3a)** binds with VEGFR1 throughout the MDS up to 100ns (**d**), RMSD for compound **3a** and represented graphically with VEGFR1 active site residues (**e**). (For interpretation of the references to color in this figure legend, the reader is referred to the Web version of this article.)

$$\Delta G_{(bind)} = E_{complex}(\text{minimized}) - \left[E_{ligand}\ (\text{minimized}) + E_{receptor}\ (\text{minimized})\right]$$

Where ΔG_{Bind} is binding free energy and $E_{complex}$(minimized), E_{ligand}(minimized), and $E_{receptor}$(minimized) are minimized energies of receptor-ligand complex, ligand, and receptor, respectively [41]. Where $E_{complex}$(minimized), E_{ligand}(minimized), and $E_{receptor}$(minimized) are the minimized energies of the receptor-ligand complex, ligand, and receptor, respectively, ΔG_{Bind} is the binding free energy.

2.6. Molecular dynamic simulations (MDSs)

This study conducted MDSs on a 64-bit Ubuntu 20.04 platform in the Maëstro 9.1 software. The molecular docking scores for VEGFR1, VEGFR2, EGFR, Tubulin, HTNF-α, and COX2 with top-scored ligands, which were verified by MM/GBSA, were imported and analyzed into MDSs. The docked protein-ligand complex was socked using the TIP3P water model using the system-builder option in the solvated orthorhombic periodic boundary of the box. To neutralize the complex, charges were added to each respective protein-ligand complex. The Desmond program's default relaxation technique was used to perform MDSs and a periodic boundary condition in the number of atoms, pressure, and temperature (NPT) ensemble, 310K as the temperature and 1 atm as the pressure. The RMSD, RMSF, and total energy of the complexes were examined using event analysis and simulation-interaction diagrams. The simulation was done for up to 100 ns [42].

2.7. Crystallization

2.7.1. XRD diffraction analysis

A single crystal measuring approximately 0.23 × 0.22 × 0.21 mm was selected for examination through single crystal X-ray diffraction (XRD). Rigaku XtaLAB mini diffractometer, equipped with Mo$K\alpha$ radiation (wavelength 0.71073 Å), was employed for intensity data collection. CrystalClear [43] program processed the data, and the crystal structure was determined using the direct method with SHELXS-97. SHELXL-97 refined the structure against F2 via full matrix least-squares technique, refining all non-hydrogen atoms anisotropically [44]. Hydrogen atoms were placed in geometrically acceptable positions, riding on their parent atoms.

The refinement involved 479 parameters with 8156 unique reflections. After several cycles, it terminated upon the residual factor converging to R = 0.0693. The weight factor w$R2$ was 0.1454, and the goodness-of-fit S was 1.044. Geometrical calculations utilized PLATON [45], and MERCURY software [46] generated ORTEP and molecular packing diagrams. The asymmetric unit comprises two molecules, A and B. Fig. 2 displays the ORTEP of the compound with molecules A and B at a 50 % probability. Crystal data and structure refinement details are provided in Table 1, while Tables 2 and 3, and 4 list bond lengths, bond angles, and torsion angles, respectively (see Table 4).

3. Results and discussions

3.1. Chemistry

The synthesis of the target compounds (**3a-c**) is illustrated in Scheme 1. The elucidation of the chemical structure for the recently synthesized compounds were accomplished through a comprehensive analysis of IR, ^{1}H and LC-MS spectroscopic data. The creation of the compound was verified by noting the absence of compounds (**1** and **2**) –CHO and –CO– stretching bands and the emergence of a new stretching band for the CH═CH group within the IR absorption spectrum, specifically at 1593 cm^{-1}, indicative of the ester group. The ^{1}H NMR spectrum of compound (**3a**) stands out as a distinctive representation, highlighting key features crucial for deducing the final molecular structure. Effortlessly discernible in the spectrum is the conspicuous absence of protons associated with aldehyde and ketone groups in compounds (**1** and **2**). Simultaneously, the emergence of two distinctive protons attributed to the CH═CH moiety is evident at chemical shifts δ 7.91 and 8.39 and ppm [9]. This spectral transformation serves as a compelling indication of the successful formation of compound (**3**). Further confirmation is derived from the mass spectrum, which exhibits a prominent and stable M+1 peak at m/z 359. This significant observation not only reinforces the proposed molecular structure but also adds credence to the authenticity of the synthesized compounds, thus solidifying its characterization as the intended title compounds (**3a-c**) (**Supplementary S1**– **S8**).

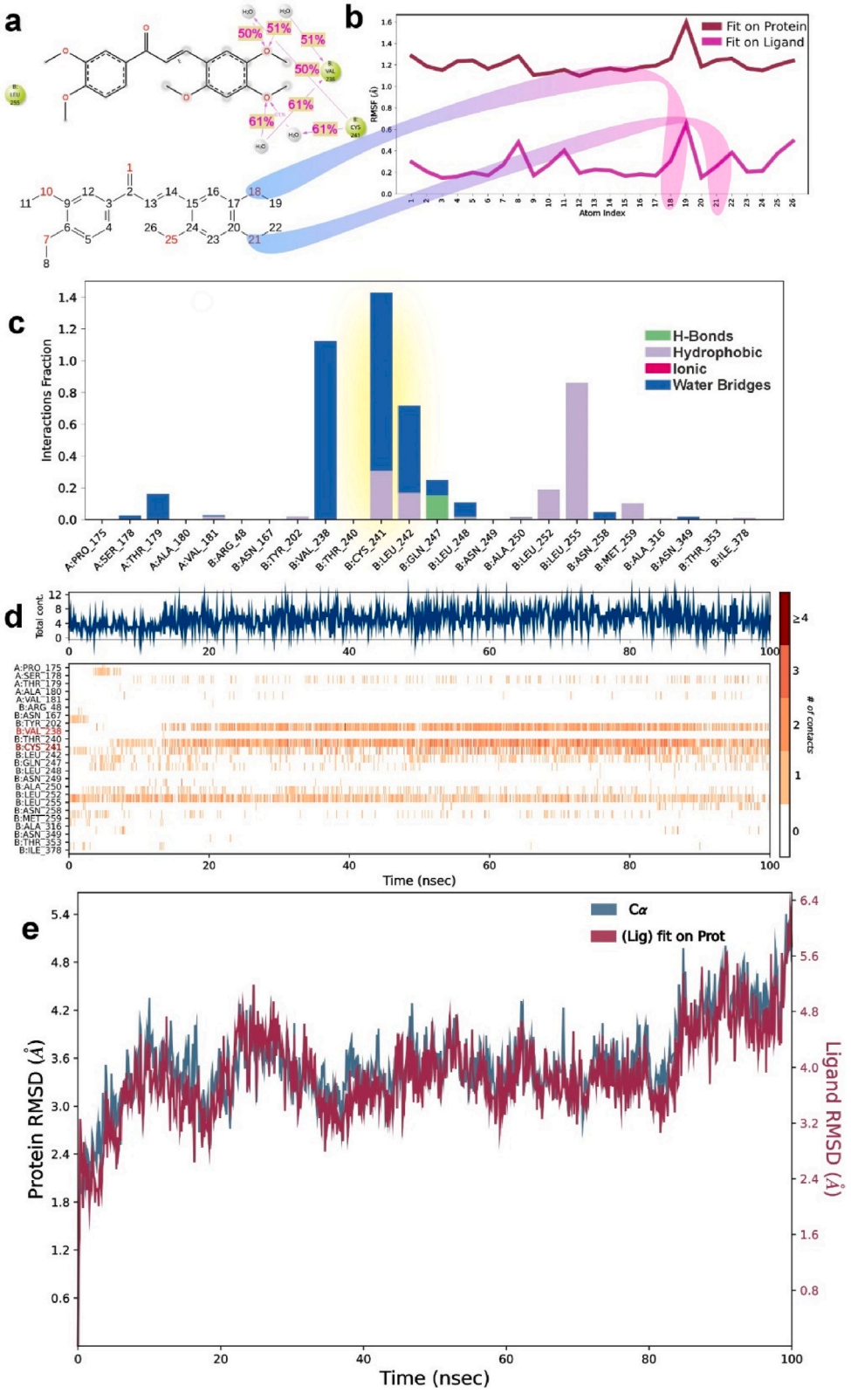

(caption on next page)

Fig. 12. 2D geometrical interactive plot showing interactions of amino acids with chemical **3a** in 2D binding view at the potential tubulin binding site **3a** (**a**) and L-RMSF depicting the atoms from the compound **(3a)** interacting with the tubulin throughout the MDSs (**b**) and the type of interaction possessed by the protein-ligand complex is summarized in a normalized stacked bar chart (**c**). The number of contact strengths is color-coded, which represents that the compound **(3a)** binds with tubulin throughout the MDS up to 100ns (**d**), RMSD for compound **3a** represented graphically with tubulin active site residues (**e**). (For interpretation of the references to color in this figure legend, the reader is referred to the Web version of this article.)

3.2. Crystal structure description

The single crystal XRD study revealed that the compound crystallizes in the triclinic crystal system in the P-1 space group. The geometrical parameters are: a = 11.8054(19)Å, b = 12.332(2)Å, c = 14.291(3)Å, α = 72.139°, β = 69.142°, γ = 76.583°, and volume is 1832.8(6)Å^{-3}.

The trimethoxyphenyl ring (C3A-C8A) is nearly planar with a maximum deviation of 0.009(3)Å for atom C8A. Additionally, it is demonstrated by the torsion angle values of O2A-C3A-C8A-C7A = 178.9(2)°, C4A-C3A-C8A-C7A = 1.3(4)°, C4A-C3A-C8A-C13A = 179.9(2)°, and C5A-C5A-C4A-C3A = 0.2(4)°. The maximum deviation for C19A from the dimethoxy ring is 0.015(3)Å. The carbonyl group makes an angle of −7.0(3)° for O16A-C15A-C17A-C22A atoms with the 3,4 dimethoxyphenyl ring indicating that they are in -*syn*-periplanar conformation. The bond length of 1.225(3)Å confirms the existence of C═O in the structure.

The bond angles of the dimethoxy and trimethoxy rings lie in the range of 117.9(2)° to 122.0(3)° indicating the nearly trigonal conformation or sp^2 hybridization of these rings. The maximum variation of dimethoxyphenyl ring (C17A-C22A) is 0.015(3)Å for C19A. The C═C bond length in prop-2-en-1-one (C13A-C14A) is 1.320(4)Å. The two rings in the molecule are sp^2 hybridized. The 3,4-trimethoxy-phenyl ring (C3B–C8B) is nearly planar with a maximum deviation of 0.015(3)Å for atom C4B. It is also evident by the torsion angle values of C8B–C3B–C4B–C5B = 1.3(3)°, O2B–C3B–C4B–C5B = 178.6(2)°, C4B–C5B–C6B–C7B = −2.6(4)°, and O9B–C5B–C6B–C7B 177.1(2)°.

The bond length of 1.230(3)Å confirms the existence of C═O in the structure. The di-methoxy ring (C17B–C22B) is planar with a maximum r.m.s. deviation of 0.010(3)Å for C20B. The bond angles of the dimethoxy and trimethoxy rings lie in the range of 117.9(2)° to 122.0(3)° indicating the nearly trigonal conformation or sp^2 hybridization of these rings. The ring (C15B–C20B) is slightly deviated from the pyridine ring making a dihedral angle of 178.6(2)°, indicating the planar conformation of the rings. The molecular packing of the compound viewed down along the a axis is shown in Fig. 3. The intermolecular C–H···O hydrogen bonds form supramolecular assembly which links a pair of molecules.

3.3. Molecular packing and supramolecular assembly

Intramolecular C–H···O hydrogen bonds are observed in the molecular structure which enhance the structural stability of the compound. The various hydrogen bond interactions along with the geometry/symmetry details are listed in Table 5.

The crystal structure is further reinforced by edge-to-face, C–H … π stacking interactions. The significant C–H … π interactions start around 2.88 Å-2.99 Å with small slip angles ($\gamma < 15°$). The details of the same are listed in Table 6. The structure is further stabilized by both medium to weak and medium to strong π-π stacking interactions as they show small centroid-centroid distance (cg … cg < 4.0 Å) with small slip angles ($\beta, \gamma < 30°$) and (cg … cg > 4.0 Å) with large slip angles ($\beta, \gamma > 30°$), Table 7 [47].

3.4. Hirshfeld surface analysis

The generation of Hirshfeld surface maps and corresponding 2D fingerprint plots was facilitated using CrystalExplorer17 [48] software. Close intermolecular contacts were highlighted on the Hirshfeld surface by computing the normalized contact distance, dnorm [49]. Fig. 4 displays the Hirshfeld surface mapped over the dnorm surface. The red regions labeled as a, b, and c indicate C12A-H12A … O16A, C1A-H1A3 … O23B, and C18A-H18A … O16B intermolecular hydrogen bond contacts, signifying strong hydrogen bonds.

Quantitative information regarding the nature and type of intermolecular interactions in the crystal structure is provided by the 2D fingerprint plots. Fig. 5 illustrate the fingerprint plots for di (distance from the nearest atom interior to the surface) and de (distance from the nearest atom external to the surface). H–H contacts, contributing significantly to the total Hirshfeld surface at 45.31 %, are represented prominently. The fingerprint plots in Fig. 5 exhibit sharp spikes corresponding to major intermolecular O–H contacts. Table 8 lists the percentage contributions of various contacts to the total Hirshfeld surface.

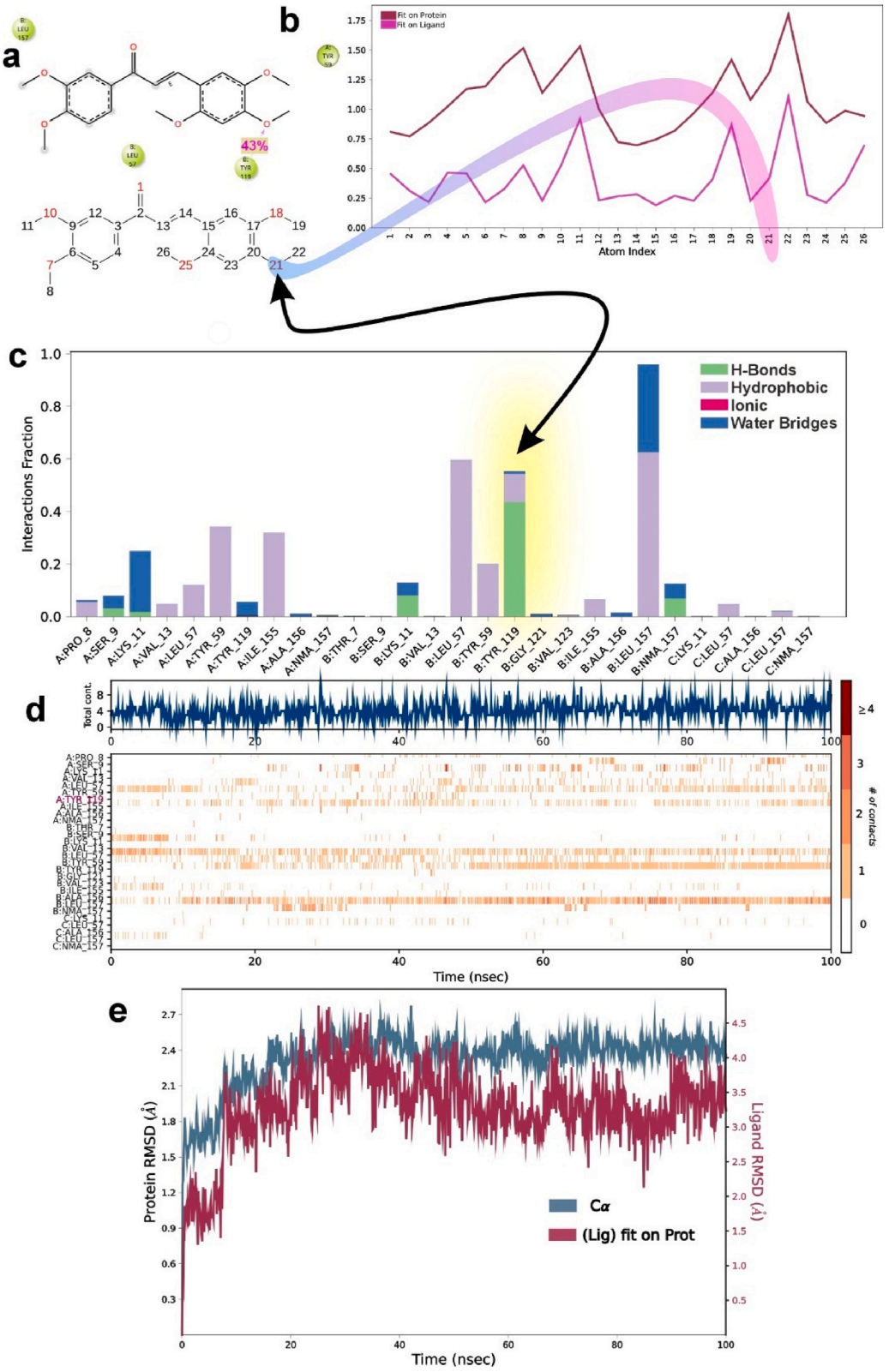

(caption on next page)

Fig. 13. 2D geometrical interactive plot showing interactions of amino acids with chemical **3a** in 2D binding view at the potential HTNF-α binding site **3a** (**a**) and L-RMSF depicting the atoms from the compound **(3a)** interacting with the HTNF-α throughout the MDSs (**b**) and the type of interaction possessed by the protein-ligand complex is summarized in a normalized stacked bar chart (**c**). The number of contact strengths is color-coded, which represents that the compound **(3a)** binds with HTNF-α throughout the MDSs up to 100ns (**d**), RMSD for compound **3a** and protein is represented graphically with HTNF-α active site residues (**e**). (For interpretation of the references to color in this figure legend, the reader is referred to the Web version of this article.)

3.5. Density functional theory (DFT)

DFT calculations were conducted to optimize the geometric coordinates, utilizing gamess-US software [50] with the hybrid functional B3LYP and a 6-31+G(d,p) basis set. The outcomes, including bond lengths, bond angles, and torsion angles, were compared with data obtained from single crystal X-ray diffraction (Tables 2 and 3, and **4**). Additionally, an analysis of the highest occupied (HOMO) and lowest unoccupied (LUMO) frontier molecular orbitals was performed. The energy gap between HOMO and LUMO was determined to be 3.10 eV, and Fig. 6 illustrates the HOMO and LUMO molecular orbitals. The value of energy gap is found to be consistent with the similar compounds reported earlier. It infers that the molecule is reactive and soft.

Examining the molecular orbitals revealed that the electron density at HOMO is entirely localized over the trimethoxy ring, while at LUMO, it is concentrated over the chalcone moiety. The orbital energy gap (ΔE) between HOMO and LUMO, along with other descriptive parameters such as electronegativity (χ), chemical potential (μ), global hardness (η), and electrophilicity index (ω), were determined and are presented in Table 9.

3.6. Topology analysis

3.6.1. Quantum theory of atoms in molecule (QTAIM)

The intramolecular interactions were explored using quantum theory of atoms in molecules (QTAIM) analysis. Atom in molecules calculations confirms the presence of intramolecular interactions which stabilize the molecular packing. AIM calculations were performed using Multiwfn software [51]. The C13A-H13A … O16A intramolecular interactions were observed from X-ray diffraction analysis and it is validated by AIM calculations, Fig. 7.

3.6.2. Electron localization function and localized orbital locator (ELF and LOL)

ELF serves as a scalar function gauging excess kinetic energy density resulting from Pauli's repulsion. In areas with weak Pauli's repulsion, ELF attains a value of unity, while it registers zero in regions with strong Pauli's repulsion. The examination of the density gradient field allows for the identification of attractive regions and their corresponding basins. The ELF and LOL analyses, which rely on kinetic energy density are carried out using Multiwfn software [51].

The resulting plots of ELF and LOL for the molecule are depicted through colored maps (see Fig. 8a and **b**). Fig. 8a illustrates the presence of high localized bonding and non-bonding electrons around hydrogen atoms, as indicated by elevated ELF regions. Delocalized electron clouds concentrated around carbon atoms are depicted by blue regions. In Fig. 8b, the white color in the central part of the hydrogen atom signifies that the electron density surpasses the color scale limit (0.80). Covalent regions between carbon-carbon atoms are predominantly red. Additionally, the blue circles around carbon atoms denote electron depletion regions between inner shell and valence shell [52].

3.6.3. Reduced density gradient

Reduced density gradient (RDG) is a dimensionless quantity, used to visualize the non-covalent interactions(NCIs). The reduced density gradient, R(r) is expressed as,

$$\mathrm{R(r)} = \frac{1}{2(3\pi^2)^{1/3}} \frac{|\nabla\rho(r)|}{\rho(r)^{4/3}}$$

where ∇ρ(r) is gradient of electron density. RDG is used to analyze the nature and strength of the interactions in the molecule [53]. The sign of λ_2 is the second largest value of hessian matrix of electron density helps to identify the nature of interactions in the molecule. The attractive interaction is observed if $\lambda 2 < 0$ and the replusive interaction is seen if $\lambda 2 > 0$. The RDG isosurface and 2D plot of ρ(r) against sign λ2 are obtained using Multiwfn [51] and VMD [54] softwares (Fig. 9). The RDG analysis was carried out at isosurface value of 0.5. The repulsive interactions are observed in the centers of dimethoxy and trimethoxy rings. The green color with slight brown color shows the weak van der Waals's attractive interactions due to hydrogen-hydrogen interactions.

3.6.4. Molecular electrostatic potential (MEP)

MEP map is very helpful in the analysis of the correlation, molecular structures with its physiochemical property relationship, including biomolecules and drugs [55]. MEP map of the compound is shown in Fig. 10. The electrostatic potentials are represented by

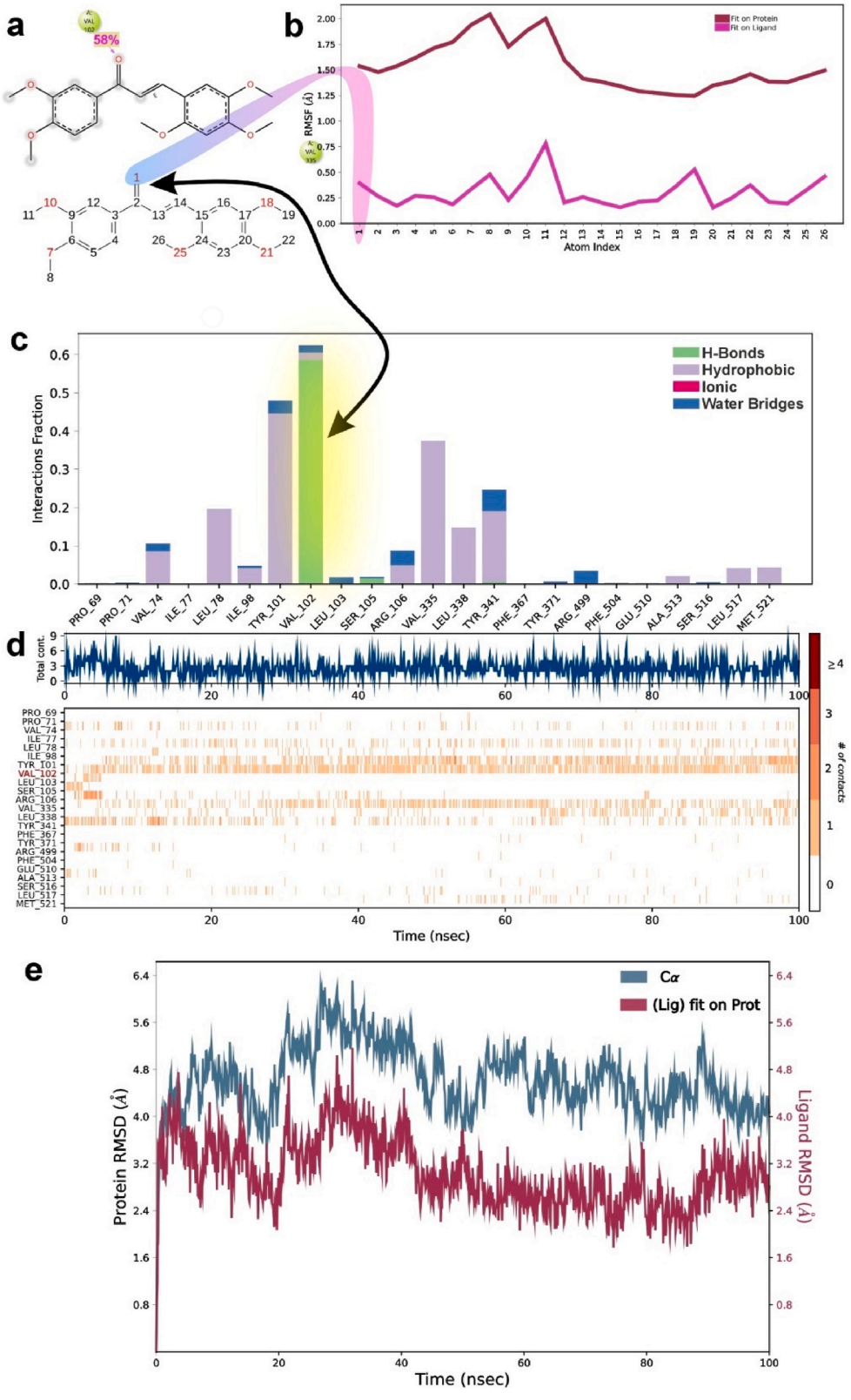

(caption on next page)

Fig. 14. 2D geometrical interactive plot showing interactions of amino acids with chemical **3a** in 2D binding view at the potential COX2 binding site **3a** (**a**) and L-RMSF depicting the atoms from the compound **(3a)** interacting with the COX2 throughout the MDSs (**b**) and the type of interaction possessed by the protein-ligand complex is summarized in a normalized stacked bar chart (**c**). The number of contact strengths is color-coded, which represents that the compound **(3a)** binds with COX2 throughout the MDS up to 100ns (**d**), RMSD for compound **3a** represented graphically with COX2 active site residues (**e**). (For interpretation of the references to color in this figure legend, the reader is referred to the Web version of this article.)

different coloring codes. On the MEP map, the red color represents the regions of the most negative electrostatic potential, while blue color represent the regions of the most positive electrostatic potential. The potential on the surface varies in the increasing order as red, orange, yellow, green, cyan, blue colors. Positive and negative regions of electrostatic potential are associated with nucleophilic (blue) and electrophilic (red) reactive sites. The MEP map shows that the negative potential sites are observed on oxygen and the positive potential sites are seen around the hydrogen atoms. The interactions supports the results from X-ray diffraction studies, which helps to the molecular packing.

3.7. In silico studies

Compounds **(3a-c)** are highly effective against VEGFR1, VEGFR2, EGFR, Tubulin, HTNF-α, and COX2 through a molecular docking study. Conversely, the compounds (**3a** and **3c**) are very potent against VEGFR1, VEGFR2, EGFR, Tubulin, HTNF-α, and COX2, as listed in Table 10. Compound (**3a**) showed a maximum G_{score} of HTNF-α (−9.81 kcal/mol); Tubulin (−7.96 kcal/mol); COX2 (−7.88 kcal/mol), EGFR (−6.72 kcal/mol), and VEGFR1(−2.50 kcal/mol). Where compound (**3c**) showed maximum binding at the putative binding site with dock scores for VEGFR2 (−9.24 kcal/mol). Hence, the molecular mechanics was done for all the compounds to verify the molecular docking. The protein-ligand complexes with greater binding energies were pulled down further to evaluate the efficiencies of MM/GBSA.

3.8. MM/GBSA

The G_{score} for each ligand was calculated against VEGFR1, VEGFR2, EGFR, Tubulin, HTNF-α, and COX2 to validate the molecular docking method and forecast how the ligand-protein complex would behave. The MM/GBSA score is continuously used to validate the outcomes of molecular docking. The biological activity data from a varied set is usually linked with MM/GBSA scoring for an independent ligand against the targeted macromolecule [56]. The results of the MMGBSA were quantified in terms of the $\Delta G_{(binding\ energy)}$, $\Delta G_{(Coulomb)}$, $\Delta G_{Covalent\ energy)}$, $\Delta G_{(H\text{-}bond)}$, $\Delta G_{(Lipo)}$, and $\Delta G_{(vdW)}$ involved (Table 10). Compound (**3a**) binds to VEGFR1 (ΔG_{Bind} −22.26 kcal/mol), Tubulin (ΔG_{Bind} −59.57 kcal/mol), HTNF-α (ΔG_{Bind} −29.02 kcal/mol), EGFR (ΔG_{Bind} −5.66 kcal/mol), and COX2 (ΔG_{Bind} −41.49 kcal/mol) Table 10). Whereas compound (**3c**) binds to VEGFR2 (ΔG_{Bind} −61.05 kcal/mol). Among the series, compound (**3c**) interaction with EGFR is found to be very weak with total ΔG energies. The individual protein-ligand complexes with good binding energies were subjected to MDSs to study the protein and ligand molecular dynamics.

3.9. Molecular dynamics simulations

MDSs for each docked complex to study the molecular dynamics of each selected ligand against the targeted macromolecule [57, 58]. When compound **(3a)** is bound to VEGFR1, it forms a hydrogen bond with Lys850 (Fig. 11a). The 21st oxygen atom of compound (**3a**) forms a bound with a strength of 53 % which is represented by the L-RMSD plot wherein the protein fit and ligand fit are closely communicated (Fig. 11b). The various interactions between compound (**3a**) and VEGFR1 are given by a normalized stacked bar chart compound (**3a**) majorly forms hydrogen bonds and water bridges with Lys850 and other minor interactions with Lys851, Leu889, and Leu895 with form hydrophobic interactions and hydrogen bonds (Fig. 11c). During MDSs how these amino acids interact with the compound (**3a**) is given by the timeline graph which shows that Lys850 forms good interaction with (**3a**) throughout the 100 ns simulation time (Fig. 11d). To figure out the stability of the compound (**3a**) and VEGFR1, a Protein-ligand RMSD plot shows stable fluctuations within the permissible limit and suggests that the compound **3a**-VEGFR1 complex is stable (Fig. 11e).

Compound (**3a**) binds to the tubulin B-chain just near the junction of A and B-chain (Fig. 12a). The L-RMSF for compound **(3a)** with tubulin provides a valuable pharmacophore mapping (Fig. 12b) with ligand interactions with the polypeptide which suggests that the atoms no 18 and 21 interact with the Val238 and Cys241 via catalytical water molecules. Fig. 12c and **d** represent the active amino acids such as Val238 and Cys241 form continuous interaction throughout the simulation and data is represented in a normalized stacked bar chart of the compound (**3a**) interacting with tubulin, primarily by water bridges and hydrophobic interactions. The protein and ligand RMSD are stable and remain stable throughout the MDSs (Fig. 12e).

Compound (**3a**) binds to the HTNF-α via a hydrogen bond strength of 43 % with Tyr119 (Fig. 13a). The L-RMSF for compound **(3a)** with HTNF-α shows that atom no 21 of compound (**3a**) is aiding interaction with Tyr119 (Fig. 13b). The type of interaction and the stability of the protein-ligand complex are stable throughout the MDSs (Fig. 13c, and **d).**

Whereas with COX2, the atom no 1 of compound (**3a**) was found to have a good hydrogen bond interaction via Val102 with a strength of 58 % (Fig. 14a and **b**), and the interaction is found to be a continuous interaction (Fig. 4c and **4d**). The COX2 and compound

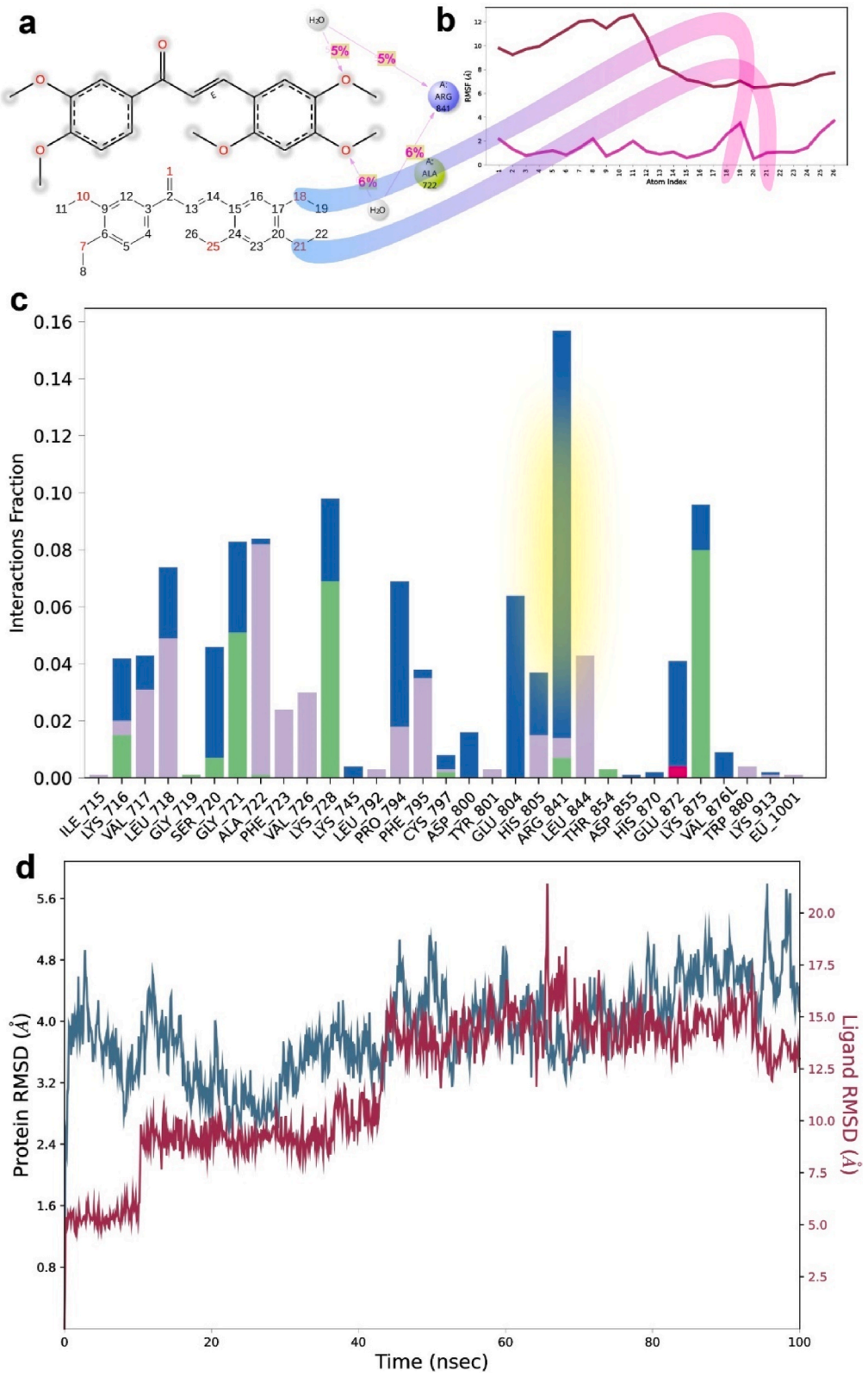

(caption on next page)

Fig. 15. 2D geometrical interactive plot showing interactions of amino acids with chemical **3a** in 2D binding view at the potential EGFR binding site **3a** (**a**) and L-RMSF depicting the atoms from the compound **(3a)** interacting with the EGFR throughout the MDSs (**b**) and the type of interaction possessed by the protein-ligand complex is summarized in a normalized stacked bar chart (**c**). The RMSD for compound **3a** is represented graphically with EGFR active site residues (**d**).

(**3a**) complex is stable throughout the MDSs and fluctuations encountered in the protein-ligand RMSD plot are within the permissible limit (Fig. 14e) [58]. Whereas with EGFR, compound (**3a**) fairly binds (Fig. 15), with Arg841 with a strength of 5 % which is the least among the reported proteins (Fig. 15a) and the L-RMSD plot suggests that the atom no 18 and 21 of (**3a**) least binds with Arg841 via (Fig. 15b) forming a water bridge (Fig. 15c). EGFR-3a complex is fairly stable after 50 ns with major fluctuations in ligand RMSD as observed in the plot (Fig. 15d).

The 2D interaction of compound (**3c**) with VEGFR2 shows π-π stacking with Phe1047 with a strength of 41 % and with Cys919 it creates a hydrogen bond that has a 96 % strength (Fig. 16a) with an oxygen atom present at the 1st position, as shown in the L-RMSF (Fig. 16b). During the MDSs with the **3c**-VEGFR2, it was found that the amino acids such as Cys919 (hydrogen bond), Phe1047, and Ala866, (hydrophobic interaction), constantly formed bonds with compound **(3c)** as shown in Figures 116c and **6d**. Protein RMSD and ligand RMSD for the complex 3c- VEGFR2 were stable and fluctuations were within permissible limits (Fig. 16e).

4. Conclusion

The synthesis of chalcone compounds (**3a-c**) yielded promising results, with the compound crystallizing in the triclinic crystal system with space group P-1. Its structure is stabilized by C– H···O and weak π-π interactions, as confirmed by Hirshfeld surface study, with H–H interactions dominating the surface. The energy band gap of 3.10 eV suggests enhanced chemical stability. The MEP map highlights the oxygen atom of the dimethoxy group as having the highest negative potential, while hydrogen atoms exhibit the highest positive potential. Covalent regions between carbon-carbon atoms were observed through ELF and LOL analyses, while RDG analysis indicates repulsive and van der Waals interactions within the molecule. Molecular docking identifies the compound (**3a**) showed a maximum G_{score} of HTNF-α (−9.81 kcal/mol); Tubulin (−7.96 kcal/mol); COX2 (−7.88 kcal/mol), EGFR (−6.72 kcal/mol), and VEGFR1(−2.50 kcal/mol). Where compound (**3c**) showed maximum binding at the putative binding site with dock scores for VEGFR2 (−9.24 kcal/mol) indicating promise as an anti-angiogenic agent.

Data availability statement

The data reported in this paper have been deposited with CCDC-1943076 contains the supplementary crystallographic data. These data can be obtained free of charge via https://www.ccdc.cam.ac.uk/structures/or by e-mailing data_request@ccdc.cam.ac.uk or by contacting The Cambridge Crystallographic Data Centre, 12 Union Road, Cambridge CB2 1EZ, UK; fax: +44(0)1223–336033.

CRediT authorship contribution statement

Fares Hezam Al-Ostoot: Writing – review & editing, Writing – original draft, Visualization, Supervision, Software, Project administration, Methodology, Investigation, Formal analysis, Data curation, Conceptualization. **P. Akhileshwari:** Writing – original draft, Visualization, Validation, Software, Methodology, Investigation, Formal analysis, Data curation, Conceptualization. **Vivek Hamse Kameshwar:** Investigation, Methodology, Software, Validation, Visualization, Writing – original draft. **D.V. Geetha:** Writing – original draft, Visualization, Validation, Software, Methodology, Investigation, Formal analysis, Data curation. **Majed S. Aljohani:** Writing – review & editing, Visualization, Validation, Methodology, Investigation, Formal analysis, Data curation. **Hussam Y. Alharbi:** Writing – review & editing, Visualization, Validation, Methodology, Investigation, Data curation. **Shaukath Ara Khanum:** Writing – review & editing.

Declaration of competing interest

The authors declare that they have no known competing financial interests or personal relationships that could have appeared to influence the work reported in this paper.

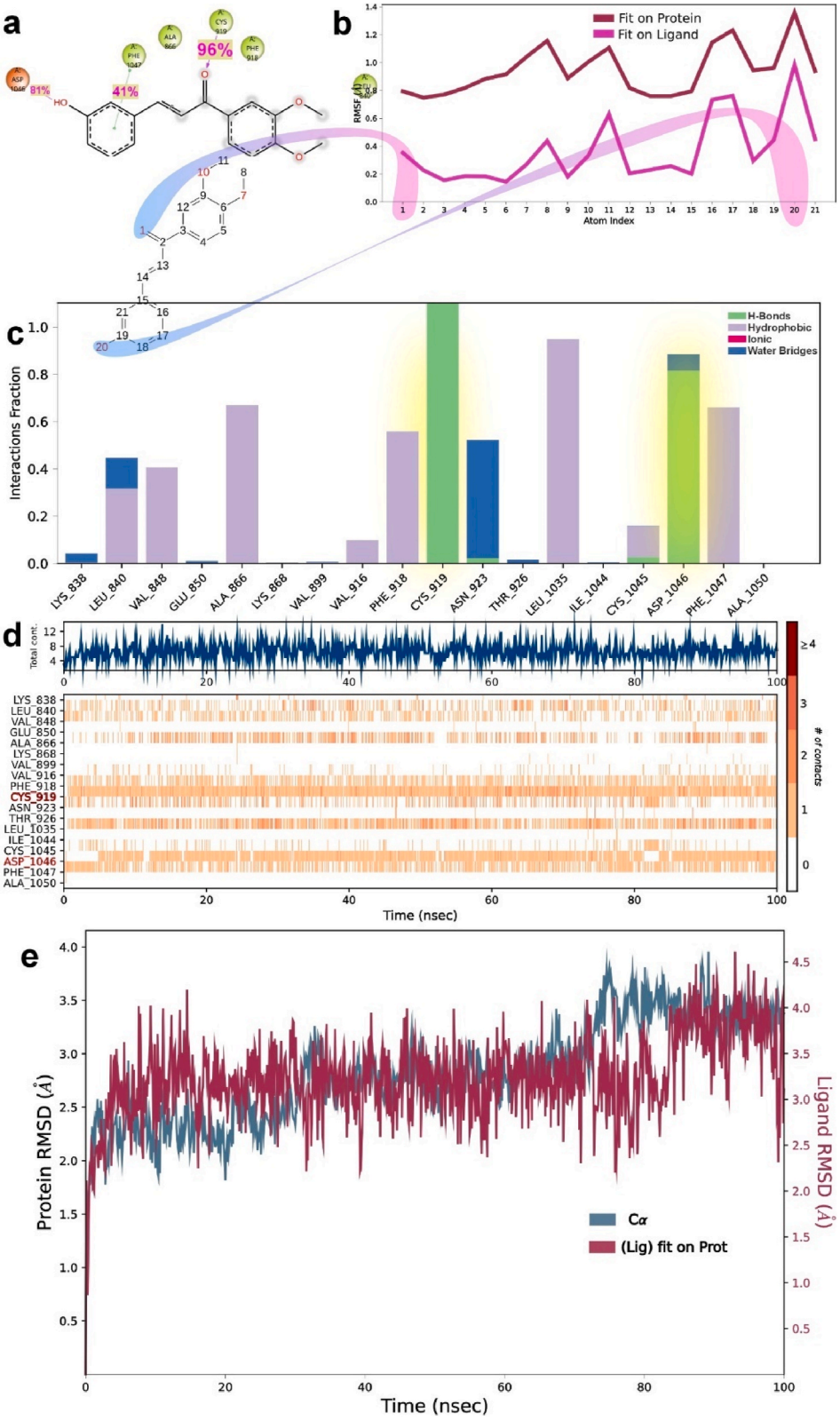

(caption on next page)

Fig. 16. 2D geometrical interactive plot showing interactions of amino acids with chemical **3c** in 2D binding view at the potential VEGFR2 binding site **3c** (**a**) and L-RMSF depicting the atoms from the compound **(3c)** interacting with the VEGFR2 throughout the MDSs (**b**) and the type of interaction possessed by the protein-ligand complex is summarized in a normalized stacked bar chart (**c**). The number of contact strengths is color-coded, which represents that the compound **(3c)** binds with VEGFR2 throughout the MDS up to 100ns (**d**), RMSD for compound **3c** represented graphically with VEGFR2 active site residues (**e**). (For interpretation of the references to color in this figure legend, the reader is referred to the Web version of this article.)

Acknowledgement

Fares Hezam Al-Ostoot are thankful to the government of Albaydha University, Yemen. Akhileshwari P thanks to DST-KSTePS, Government of Karnataka, Bengaluru.

Appendix A. Supplementary data

Supplementary data to this article can be found online at https://doi.org/10.1016/j.heliyon.2024.e33814.

References

[1] D.M. Parkin, The global health burden of infection-associated cancers in the year 2002, Int. J. Cancer 118 (12) (2006) 3030–3044.
[2] M. Wangen, C. Escoffery, M.E. Fernandez, D.B. Friedman, P. Hannon, L.K. Ko, A.E. Maxwell, C. Petagna, B. Risendal, C. Rohweder, J. Leeman, Twenty years of capacity building across the cancer prevention and control research network, Cancer Causes & Control 34 (2023) 45–56.
[3] Y. Brown, S. Hua, P.S. Tanwar, Extracellular matrix in high-grade serous ovarian cancer: advances in understanding of carcinogenesis and cancer biology, Matrix Biol. 118 (2023) 16–46.
[4] F.H. Al-Ostoot, A. Sherapura, V.H. Malojirao, P. Thirusangu, T.I. Al-Muhimeed, S.A. Khanum, B.T. Prabhakar, Modulation of DNA damage response by targeting ATM kinase using newly synthesized di-phenoxy acetamide (DPA) analogs to induce anti-neoplasia, Pharmacol. Rep. 73 (5) (2021) 1344–1360.
[5] A. Laruelle, A. Rocha, C. Manini, J.I. López, E. Inarra, Effects of heterogeneity on cancer: a game theory perspective, Bull. Math. Biol. 85 (8) (2023) 72.
[6] Y. Qin, M. Ashrafizadeh, V. Mongiardini, B. Grimaldi, F. Crea, K. Rietdorf, B. Győrffy, D.J. Klionsky, J. Ren, W. Zhang, X. Zhang, Autophagy and cancer drug resistance in dialogue: pre-clinical and clinical evidence, Cancer Lett. 570 (2023) 216307.
[7] K. Mezgebe, Y. Melaku, E. Mulugeta, Synthesis and pharmacological activities of chalcone and its derivatives bearing N-heterocyclic scaffolds: a review, ACS Omega 8 (22) (2023) 19194–19211.
[8] S.M. Kumar, B.C. Manjunath, F.H. Al-Ostoot, M. Jyothi, M. Al-Ghorbani, S.A. Khanum, A.K. Kudva, N.K. Lokanath, K. Byrappa, Synthesis, crystal structure and Hirshfeld surfaces of 1-(3, 4-dimethoxyphenyl)-3-(3-hydroxyphenyl) prop-2-en-1-one, Chem. Data Collect. 15 (2018) 153–160.
[9] S.M. Kumar, A.O. Hezam, B.C. Manjunath, V.R. Shamprasad, Y.H. Mohammed, N. Mahesh, A.K. Shaukath, N.K. Lokanath, K. Byrappa, Crystal packing analysis of 1-(3, 4-dimethoxyphenyl)-3-(4-bromophenyl) prop-2-en-1-one exhibiting a putative halogen bond CBr··· O, J. Mol. Struct. 1156 (2018) 216–223.
[10] H. Wang, J. Zhu, Q. Zhang, J. Tang, X. Huang, Current scenario of chalcone hybrids with antibreast cancer therapeutic applications, Arch. Pharm. 357 (5) (2024) e2300640.
[11] G.B. Souza, T.A. Santos, A.P. Silva, A.L. Barreiros, V.B. Nardelli, I.B. Siqueira, S.S. Dolabella, E.V. Costa, P.B. Alves, R. Scher, R.P. Fernandes, Synthesis of chalcone derivatives by Claisen-Schmidt condensation and in vitro analyses of their antiprotozoal activities, Nat. Prod. Res. 38 (8) (2022) 1326–1333.
[12] A. Tiwari, A. Bendi, A.S. Bhathiwal, An overview on synthesis and biological activity of chalcone derived pyrazolines, ChemistrySelect 6 (45) (2021) 12757–12795.
[13] H.Ç. Onar, E.M. Özden, H.D. Taslak, İ. Gülçin, A. Ece, E. Erçağ, Novel coumarin-chalcone derivatives: synthesis, characterization, antioxidant, cyclic voltammetry, molecular modelling and biological evaluation studies as acetylcholinesterase, α-glycosidase, and carbonic anhydrase inhibitors, Chem. Biol. Interact. 383 (2023) 110655.
[14] S. Narwal, B. Devi, T. Dhanda, S. Kumar, S. Tahlan, Exploring chalcone derivatives: synthesis and their therapeutic potential, J. Mol. Struct. 1303 (2024) 137554.
[15] R. Pereira, A.M. Silva, D. Ribeiro, V.L. Silva, E. Fernandes, Bis-chalcones: a review of synthetic methodologies and anti-inflammatory effects, Eur. J. Med. Chem. 252 (2023) 115280.
[16] N. Zhang, W. Zeng, Q. Zhou, Z. Sun, K. Meng, Y. Qin, Y. Hu, W. Xue, Design, synthesis, antibacterial and antiviral evaluation of chalcone derivatives containing benzoxazole, Arabian J. Chem. 17 (1) (2024) 105368.
[17] F.H. Al-Ostoot, Zabiulla, S. Salah, S.A. Khanum, Recent investigations into synthesis and pharmacological activities of phenoxy acetamide and its derivatives (chalcone, indole and quinoline) as possible therapeutic candidates, J. Iran. Chem. Soc. 18 (2021) 1839–1875.
[18] J. Knockleby, A.D. Djigo, I.K. Lindamulage, C. Karthikeyan, P. Trivedi, H. Lee, Lead optimization of novel quinolone chalcone compounds by a structure–activity relationship (SAR) study to increase efficacy and metabolic stability, Sci. Rep. 11 (1) (2021) 21576.
[19] H. Şenol, M. Ghaffari-Moghaddam, G.Ö. Toraman, U. Güller, Novel chalcone derivatives of ursolic acid as acetylcholinesterase inhibitors: synthesis, characterization, biological activity, ADME prediction, molecular docking and molecular dynamics studies, J. Mol. Struct. 1295 (2024) 136804.
[20] H.A. Khamees, M. Madegowda, S. Ananda, Y. Sangappa, F.H. Al-Ostoot, N. Abad, Synthesis, molecular structure, DFT studies, in silico docking and molecular dynamics simulations of 2, 6 dimethoxychalcone derivatives as BRD4 inhibitors, J. Mol. Struct. 1245 (2021) 131032.
[21] H. Avci, H. Gunduz Altintas, Y. Yildiz, D. Coskun, F. Ari, Effects of chalcone derived compounds on cell cycle and migration capability of human breast and lung cancer cells, Biol. Bull. 50 (5) (2023) 749–760.
[22] M. Kello, D. Drutovic, M.B. Pilatova, V. Tischlerova, P. Perjesi, J. Mojzis, Chalcone derivatives cause accumulation of colon cancer cells in the G2/M phase and induce apoptosis, Life Sci. 150 (2016) 32–38.
[23] H. Avci, H. Gunduz Altintas, Y. Yildiz, D. Coskun, F. Ari, Effects of chalcone derived compounds on cell cycle and migration capability of human breast and lung cancer cells, Biol. Bull. 50 (5) (2023) 749–760.
[24] S.R. Nayak, L.S. Dhivya, R. Reshma, B.O. Almutairi, S. Arokiyaraj, M.K. Kathiravan, J. Arockiaraj, Furan based synthetic chalcone derivative functions against gut inflammation and oxidative stress demonstrated in in-vivo zebrafish model, Eur. J. Pharmacol. 957 (2023) 175994.
[25] F.H. Al-Ostoot, S. Salah, H.A. Khamees, S.A. Khanum, Tumor angiogenesis: current challenges and therapeutic opportunities, Cancer Treat. Res. Commun. 28 (2021) 100422.
[26] S. Burmaoglu, A. Gobek, D.A. Anil, M.A. Alagoz, A. Guner, C. Güler, C. Hepokur, N.U. Karabay Yavasoglu, O. Algul, Assessing the antiangiogenic effects of chalcones and their derivatives, Polycyclic Aromat. Compd 44 (1) (2024) 51–66.
[27] L. Deng, J. Qu, Synthesis and properties of novel bis-chalcone-based photoinitiators for LED polymerization with photobleaching and low migration, Prog. Org. Coat. 174 (2023) 107240.

[28] F.H. Al-Ostoot, D.V. Geetha, Y.H. Mohammed, P. Akhileshwari, M.A. Sridhar, S.A. Khanum, Design-based synthesis, molecular docking analysis of an anti-inflammatory drug, and geometrical optimization and interaction energy studies of an indole acetamide derivative, J. Mol. Struct. 1202 (2020) 127244.
[29] F.H. Al-Ostoot, S. Grisha, Y.H. Mohammed, H.K. Vivek, S.A. Khanum, Molecular docking and synthesis of caffeic acid analogous and its anti-inflammatory, analgesic and ulcerogenic studies, Bioorg. Med. Chem. Lett. 33 (2021) 127743.
[30] S.N. Chandana, F.H. Al-Ostoot, Y.H. Mohammed, T.N. Al-Ramadneh, P. Akhileshwari, S.A. Khanum, M.A. Sridhar, B.N. Lakshminarayana, Synthesis, structural characterization, and DFT studies of anti-cancer drug N-(2-Aminophenyl)-2-(4-bromophenoxy) acetamide, Heliyon 7 (3) (2021) e06464.
[31] V. Asati, P. Ghode, S. Bajaj, K.S. Jain, K.S. Bharti, 3D-QSAR and molecular docking studies on oxadiazole substituted benzimidazole derivatives: validation of experimental inhibitory potencies towards COX-2, Curr. Comput. Aided Drug Des. 15 (4) (2019) 277–293.
[32] V. Asati, S.S. Thakur, N. Upmanyu, S.K. Bharti, Virtual screening, molecular docking, and DFT studies of some thiazolidine-2,4-diones as potential PIM-1 kinase inhibitors, ChemistrySelect 3 (1) (2018) 127–135.
[33] S. Dhiman, M. Saha, A. Ali, A. Ali, G.D. Gupta, V. Asati, Structural aspects of triazole derivatives as HSP90 inhibitors for the treatment of cancer: in silico studies, J. Biomol. Struct. Dyn. 41 (10) (2023) 4756–4769.
[34] H.K. Keerthy, H.K. Vivek, H. Bharathkumar, S. Rangappa, K.C. Bulusu, L.H. Mervin, J.E. Fuchs, B.S. Priya, Basappa, N. Swamy S, A. Bender, K.S. Rangappa, MOLPRINT 2D-based identification and synthesis of novel chromene based small molecules that target PLA2: validation through chemo- and bioinformatics approaches, RSC Adv. 5 (109) (2015) 89797–89808.
[35] M.G. Prabhudeva, H.K. Vivek, K.A. Kumar, Synthesis of novel pyrazole carboxamides using reusable catalyst as antimicrobial agents and molecular docking studies, Chem. Data Collect. 20 (2019) 100193.
[36] D. Shivakumar, J. Williams, Y. Wu, W. Damm, J. Shelley, W. Sherman, Prediction of absolute solvation free energies using molecular dynamics free energy perturbation and the OPLS force field, J. Chem. Theory Comput. 6 (5) (2010) 1509–1519.
[37] D. Das, M. Nanda, P. Banjare, S. Lanjhiyana, Exploration of multitargeted antialzheimer's activity of safflower leaves phytoconstituents: in silico molecular docking approach, Eur. J. Med. Chem. Rep 10 (2024) 100119.
[38] C. Mallick, M. Mishra, V. Asati, V. Kashaw, R. Das, S.K. Kashaw, In silico-based structural prediction, molecular docking and ADMET analysis of novel imidazo-quinoline derivatives as pf purine nucleoside phosphorylase inhibitors, Curr. Signal Transduction Ther. 18 (1) (2023) 24–53.
[39] P.A. Greenidge, C. Kramer, J.-C. Mozziconacci, R.M. Wolf, MM/GBSA binding energy prediction on the PDBbind data set: successes, failures, and directions for further improvement, J. Chem. Inf. Model. 53 (1) (2013) 201–209.
[40] J. Li, R. Abel, K. Zhu, Y. Cao, S. Zhao, R.A. Friesner, The VSGB 2.0 model: a next generation energy model for high resolution protein structure modeling, Proteins: Struct., Funct., Bioinf. 79 (10) (2011) 2794–2812.
[41] Y. Wu, L. Lou, Z.-R. Xie, A pilot study of all-computational drug design protocol–from structure prediction to interaction analysis, Front. Chem. 8 (2020) 81.
[42] K.S. Suryakoppa, K. Vivek Hamse, R. Appadurai, S. Eranna, M.H.M. Khan, Enantiomeric separation of indole-3-propanamide derivatives by using supercritical fluid chromatography on a polysaccharide-based chiral stationary phase, J. Chromatogr. Sci. 60 (7) (2022) 692–704.
[43] Y.H. Luo, J. Xu, M.L. Pan, J.F. Li, 2, 4-Dibromo-6-[(hydroxyimino) methyl] phenol, Acta Crystallogr., Sect. E: Struct. Rep. Online 67 (8) (2011) o2099.
[44] T. Beck, A. Krasauskas, T. Gruene, G.M. Sheldrick, A magic triangle for experimental phasing of macromolecules, Acta Crystallogr., Sect. D: Biol. Crystallogr. 64 (11) (2008) 1179–1182.
[45] A.L. Spek, PLATON, an integrated tool for the analysis of the results of a single crystal structure determination, Acta Crystallogr., Sect. A: Found. Crystallogr. 46 (s1) (1990) c34.
[46] C.F. Macrae, I.J. Bruno, J.A. Chisholm, P.R. Edgington, P. McCabe, E. Pidcock, L. Rodriguez-Monge, R. Taylor, J.V. Streek, P.A. Wood, Mercury CSD 2.0–new features for the visualization and investigation of crystal structures, J. Appl. Crystallogr. 41 (2) (2008) 466–470.
[47] X.J. Yang, F. Drepper, B. Wu, W.H. Sun, W. Haehnel, C. Janiak, From model compounds to protein binding: syntheses, characterizations and fluorescence studies of [Ru II (bipy)(terpy) L] 2+ complexes (bipy= 2, 2′-bipyridine; terpy= 2, 2′: 6′, 2 ″-terpyridine; L= imidazole, pyrazole and derivatives, cytochrome c), Dalton Trans. (2) (2005) 256–267.
[48] M.A. Spackman, D. Jayatilaka, Hirshfeld surface analysis, CrystEngComm 11 (1) (2009) 19–32.
[49] J.J. McKinnon, D. Jayatilaka, M.A. Spackman, Towards quantitative analysis of intermolecular interactions with Hirshfeld surfaces, Chem. Commun. 37 (2007) 3814–3816.
[50] M.W. Schmidt, K.K. Baldridge, J.A. Boatz, S.T. Elbert, M.S. Gordon, J.H. Jensen, S. Koseki, N. Matsunaga, K.A. Nguyen, S. Su, T.L. Windus, General atomic and molecular electronic structure system, J. Comput. Chem. 14 (11) (1993) 1347–1363.
[51] T. Lu, F. Chen Multiwfn, A multifunctional wavefunction analyzer, J. Comput. Chem. 33 (5) (2012) 580–592.
[52] M.K. Jayappa, P. Akhileshwari, M.A. Sridhar, L.T. Nagarajappa, S. Nagaraju, S. Raghavendra, M.D. Jayappa, Synthesis and detailed characterization of a newly synthesized chalcone, 3-(2, 5-dimethoxyphenyl)-1-(naphthalen-2-yl) prop-2-en-1-one, Eur. J. Chem. 12 (1) (2021) 69–76.
[53] A. Guerraoui, A. Djedouani, E. Jeanneau, A. Boumaza, A. Alsalme, A. Zarrouk, K.S. Salih, I. Warad, Crystal structure and spectral of new hydrazine-pyran-dione derivative: DFT enol↔ hydrazone tautomerization via zwitterionic intermediate, hirshfeld analysis and optical activity studies, J. Mol. Struct. 1220 (2020) 128728.
[54] W. Humphrey, A. Dalke, K. Schulten, VMD: visual molecular dynamics, J. Mol. Graph. 14 (1) (1996) 33–38.
[55] E. Scrocco, J. Tomasi, Electronic molecular structure, reactivity and intermolecular forces: an euristic interpretation by means of electrostatic molecular potentials, Adv. Quantum Chem. 11 (1978) 115–193.
[56] P.D. Lyne, M.L. Lamb, J.C. Saeh, Accurate prediction of the relative potencies of members of a series of kinase inhibitors using molecular docking and MM-GBSA scoring, J. Med. Chem. 49 (16) (2006) 4805–4808.
[57] K.Y. Wong, J. Gao, The reaction mechanism of paraoxon hydrolysis by phosphotriesterase from combined QM/MM simulations, Biochemistry 46 (46) (2007) 13352–13369.
[58] T.S. Lee, C. Silva López, G.M. Giambasu, M. Martick, W.G. Scott, D.M. York, Role of Mg2+ in hammerhead ribozyme catalysis from molecular simulation, J. Am. Chem. Soc. 130 (10) (2008) 3053–3064.